



HAL
open science

Adaptive octree-based finite element analysis of two- and three-dimensional indentation problems

Cédric Thieulot, Philippe Fullsack, Jean Braun

► **To cite this version:**

Cédric Thieulot, Philippe Fullsack, Jean Braun. Adaptive octree-based finite element analysis of two- and three-dimensional indentation problems. *Journal of Geophysical Research: Solid Earth*, 2008, 113 (B12), pp.B12207. 10.1029/2008JB005591 . insu-00354316

HAL Id: insu-00354316

<https://insu.hal.science/insu-00354316>

Submitted on 29 Mar 2016

HAL is a multi-disciplinary open access archive for the deposit and dissemination of scientific research documents, whether they are published or not. The documents may come from teaching and research institutions in France or abroad, or from public or private research centers.

L'archive ouverte pluridisciplinaire **HAL**, est destinée au dépôt et à la diffusion de documents scientifiques de niveau recherche, publiés ou non, émanant des établissements d'enseignement et de recherche français ou étrangers, des laboratoires publics ou privés.

Adaptive octree-based finite element analysis of two- and three-dimensional indentation problems

C. Thieulot,¹ P. Fullsack,² and J. Braun,¹

Received 16 January 2008; revised 4 July 2008; accepted 8 September 2008; published 16 December 2008.

[1] In recent years, much has been done to develop numerical tools to study the three-dimensional nature of the Earth's lithosphere deformation. DOUAR is one of them: it is a new ALE Finite Element code that is based on an adaptive grid, a key feature in the capture of localized deformation. In order to illustrate this, various simulations of punch experiments have been performed on rigid plastic materials with von Mises and Drucker-Prager type of rheologies. We present the grid refinement algorithm based on strain rate measurements and rederive the plane strain punch analytical solution which allows us to test the accuracy of our results. Various 3-D strip punches experiments with different aspect ratios show DOUAR's ability to capture complex fault patterns. We also discuss the degree to which the incompressibility and rigid plasticity constraints are satisfied. Finally, we show the results of a crustal-scale deformation experiment demonstrating the potential of the octree-based mesh refinement algorithm to solve complex three-dimensional geodynamical problems with great efficiency and accuracy.

Citation: Thieulot, C., P. Fullsack, and J. Braun (2008), Adaptive octree-based finite element analysis of two- and three-dimensional indentation problems, *J. Geophys. Res.*, 113, B12207, doi:10.1029/2008JB005591.

1. Introduction

[2] Earth's materials have interesting plastic and viscous properties [Paterson, 1978; Carter, 1975]. At or near the surface, rocks behave mostly plastically. Down to depths of order a few kilometers, the deformation of rocks is limited by friction, a behavior consistent with the Coulomb rheological law. When the temperature is a significant fraction of their melting temperature, they behave viscously [Brace and Kohlstedt, 1980]. The mechanical response of the Earth's upper crust is of prime interest to geodynamicists. It determines the response of the Earth's crust to external forces arising from the interactions among tectonic plates that make up the Earth's lithosphere and the resulting deformation patterns. Examples of such interactions include the collision of continental masses along convergent plate boundaries, the stretching of the lithosphere in continental rifts or the formation of large strike-slip faults at other plate boundaries.

[3] A proper understanding of the rheology of the crust is therefore required, as well as appropriate numerical tools to study them. In recent years much has been done to develop such tools to study the three-dimensional nature of the Earth's lithosphere deformation [Braun, 1993; Moresi and Solomatov, 1998; Govers and Wortel, 2005], but most have been hampered by an appropriate methodology to capture the very localized nature of the deformation. Indeed, several

processes acting both in the plastic (brittle) or viscous (creep) regimes lead to localization of the deformation [Poirier, 1980]. The exact nature of the processes responsible for that localization is still the matter of active debate in the geological community (Braun *et al.* [1999] and Regenauer-Lieb *et al.* [2006], among many others).

[4] To properly capture the formation and evolution of faults or shear zones is thus necessary if one wishes to represent accurately the mechanical behavior of the Earth's lithosphere. In two dimensions, this can be achieved through high resolution, uniform discretization of space (see [Fullsack, 1995] for instance) or adaptive meshing (see [Braun and Sambridge, 2002] for example). In three dimensions, uniform spatial discretisation is limited, for implicit methods, by the efficiency of the linear solver (e.g., a uniform grid of size $128 \times 128 \times 128$ is already a hard to solve grid for the hardware and the parallel direct solver that we use).

[5] While grid adaptivity certainly has shown its virtues over the past decades, it has also become clear that mesh generation can be a far more time-consuming and expensive task than the assembly and the solution of the finite element equations. In light thereof, mesh-free methods have become increasingly popular and have proved to be a valid alternative to grid-based methods. Among them, the Element Free Galerkin Method [Belytschko *et al.*, 1994] uses moving least-squares interpolants to construct trial and test functions. The method is completely element-free, arbitrary numbers of nodes can be added in the system where accuracy is needed, and it does not appear to deteriorate the solution if the placement of nodes is very irregular. This method has been recently used for the study of lower bound shakedown analysis in the case of isotropic, elastoperfectly

¹Géosciences Rennes, Université de Rennes 1, Rennes, France.

²Oceanography Department, Dalhousie University, Halifax, Nova Scotia, Canada.

plastic materials governed by von Mises' yield criterion [Chen *et al.*, 2008].

[6] Another possible approach in order to increase the accuracy of the solution, is the p version of the finite element method. As opposed to the traditional h version in which the error in the solution is reduced by refining the mesh of size h , a p version reduces the error by increasing, within a fixed mesh, the degree p of the polynomials used. This type of method has been used as well to perform shakedown analysis in the past years [Tin-Loi and Ngo, 2003; Ngo and Tin-Loi, 2007], and it has been shown that locking due to the incompressibility naturally does not occur, a common observation made in EFG too.

[7] In this article, we show how the newly developed ALE Finite Element code DOUAR ("the Earth" in Breton language) [Braun *et al.*, 2008] is well suited to study two- and three-dimensional problems that lead to strain localization by using it to solve a simple punch experiment in a rigid plastic material. We show how DOUAR's adaptive grid is a key feature in the capture of complex fault patterns and of the localized deformation in the plastic regime. We demonstrate its flexibility and efficiency in the plane-strain case as the existence of an analytical solution allows us to test the accuracy of our results. We also present results of similar problems but with more complex, three-dimensional geometries.

[8] In the following section, we recall the basics of the theory of plasticity; we then present the numerical model DOUAR with an emphasis on its dynamic grid refinement algorithm. Section 4 is concerned with two- and three-dimensional experimental setups with various parameters and geometries. Finally, we present and discuss our results in section 5.

2. Plasticity and the Punch Problem

2.1. Introduction

[9] A solid can withstand normal forces (perpendicular to a material plane across which they act), the force per unit area on that plane being called the normal stress, and shearing forces directed parallel to the material surface on which they act. The combination of both these types of forces can lead the material to elastically deform when loaded, but if the applied forces (or rather stresses) exceed a given value characteristic of the material, it then deforms permanently. One then speaks of plastic deformation. Permanent deformation that depends mainly on time of exposure to a stress, and that tend to increase significantly with time is called viscous deformation, and such materials are coined visco-(elasto-)plastic.

[10] Plasticity has been the subject of active research for the past centuries. It started with the seminal observations of 17th and 18th century scientists such as Hooke, Bernoulli, Euler, Young, Coulomb, Cauchy, and Poisson (among many others) who formalized the concepts of stress tensor and elastic moduli through the study of beams, plates, or soil foundations. Besides what is now known as the Coulomb yield criterion [Coulomb, 1773], it is only in the mid-19th century that yet another yield criterion was proposed by Tresca [1864], followed by von Mises [1913] and by Drucker and Prager [1952], to name a few of the classical

ones found in every textbook on plasticity [Kachanov, 2004].

[11] It is in the second decade of the 20th century that Prandtl developed the rudiments of the theory of plane plastic flow applied to the analysis of indentation of a semi-infinite solid by a flat-ended rigid indenter. The resulting theory of plastic slip lines was completed by Hencky in 1923 [Tanner and Tanner, 2003] and in 1930 by Geiringer [Freudenthal and Geiringer, 1958]. While the two-dimensional problem has received much attention leading to an analytical solution for the stress, pressure and velocity fields, the three-dimensional problem cannot be solved analytically.

[12] The need in the industry for giving a prescribed shape to metals (forming), combined with the advent of numerical methods in the late fifties and the increase in computational power has led to a regain of attention in the second half of the 20th century.

[13] In many physical phenomena whose behavior is described by differential equations in a well posed manner, abrupt discontinuities may develop. An example thereof is the case of plastic fracture, with discontinuous velocity, pressure, and stress fields. Since the position of these discontinuities is not known a priori, much effort has been devoted to the implementation of plastic rheologies in numerical methods [Owen and Hinton, 1980; Zienkiewicz and Taylor, 2002] and to the capture of such discontinuities by means of automatic grid refinement algorithms [Zienkiewicz *et al.*, 1995].

[14] Also, the ultimate load which a foundation can support may be calculated using bearing capacity theory. The problem of the estimation of bearing capacities factors for two- and three-dimensional, strip, square of circular shaped footings for various rheologies and loads is source of an abundant literature [Terzaghi, 1943; Frydman and Burd, 1997; Taiebat and Carter, 2002; Lee *et al.*, 2005; Erickson and Drescher, 2002; Bolton and Lau, 1993; Gourvenec *et al.*, 2006]. Analytical results have greatly improved the estimations that previously relied on empirical laws, but numerical methods, mainly by means of the Finite Element Method (FEM), remain the preferred investigation tool. Since bearing capacities problems show a strong analogy to the flat-ended indenter problem, also commonly denoted as "punch problem," the latter remains of great interest.

2.2. Saint-Venant-Levy-Mises Equations

[15] The state of stress for a three-dimensional point is defined by a matrix containing nine stress components. The nine components of the stress at any point form a second order tensor, known as the (Cauchy) stress tensor σ . The stress components can be expressed as elements of a square matrix:

$$\sigma = \begin{pmatrix} \sigma_{xx} & \sigma_{xy} & \sigma_{xz} \\ \sigma_{yx} & \sigma_{yy} & \sigma_{yz} \\ \sigma_{zx} & \sigma_{zy} & \sigma_{zz} \end{pmatrix} \quad (1)$$

Moment equilibrium demands $\sigma_{ij} = \sigma_{ji}$ so that there are only six independent stress components: three normal stresses σ_{xx} , σ_{yy} , σ_{zz} and three shear stresses σ_{xy} , σ_{xz} , σ_{yz} .

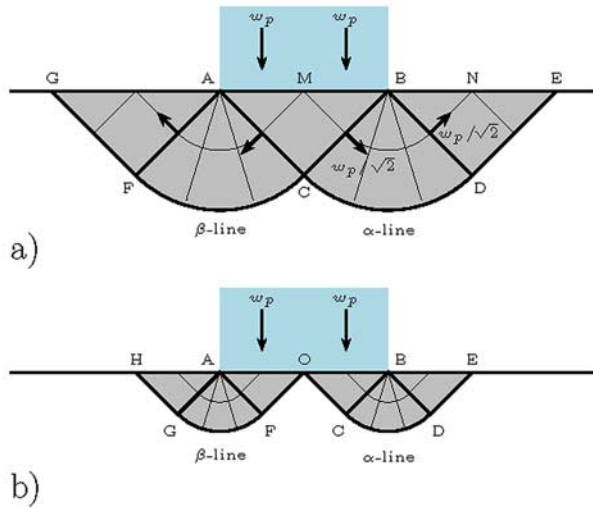


Figure 1. Two-dimensional rigid punch indenting a rigid plastic half space. (a) Prandtl's rigid plastic solution; (b) Hill's solution.

[16] One can resolve the stress tensor σ into its spherical part $p\mathbf{1}$ and into its stress deviation s as follows:

$$\sigma = -p\mathbf{1} + s \quad (2)$$

where the hydrostatic pressure is

$$p = -\frac{1}{3}(\sigma_{xx} + \sigma_{yy} + \sigma_{zz}) = -\frac{1}{3}\text{Tr}[\sigma] \quad (3)$$

The first invariant J_1 of the stress tensor and the second invariant J'_2 of its deviatoric part are defined as follows:

$$J_1 = \text{Tr}[\sigma] \quad (4)$$

$$J'_2 = \frac{1}{2}\text{Tr}[ss^T] \quad (5)$$

We present hereafter the basic equations representing the static balance of forces in a three-dimensional perfectly plastic body under the assumption of the quadratic von Mises yield criterion and of the associated stress-strain relations of Saint Venant and von Mises.

2.2.1. Strain Rate Velocity Equation

[17] The strain rate tensor is linked to the velocity field $\mathbf{v} = (u, v, w)$ as follows:

$$\dot{\epsilon} = \frac{1}{2}(\nabla\mathbf{v} + (\nabla\mathbf{v})^T) \quad (6)$$

2.2.2. Conservation of Mass

[18] Let ρ be the density of the material. The continuity equation is given by

$$\frac{d\rho}{dt} + \rho\nabla \cdot \mathbf{v} = 0 \quad (7)$$

If one takes ρ to be a constant, as assumed in the incompressible theory of perfectly plastic solids, then $d\rho/dt = 0$ and equation (7) reduces to the incompressibility condition:

$$\nabla \cdot \mathbf{v} = 0 \quad (8)$$

2.2.3. Conservation of Momentum

[19] The equation of motion takes the form

$$\rho \frac{d\mathbf{v}}{dt} = \nabla \cdot \sigma + \rho\mathbf{g} \quad (9)$$

Considering inertia-free problems yields

$$\nabla \cdot \sigma + \rho\mathbf{g} = 0 \quad (10)$$

2.2.4. Plasticity Equations

[20] The rigid plastic nature of the material translates as follows:

$$\begin{cases} \dot{\epsilon} = 0 & \Leftrightarrow F < 0 \\ \dot{\epsilon} > 0 & \Leftrightarrow F = 0 \end{cases} \quad (11)$$

where F is the yield function that is characteristic of the plasticity model [Kachanov, 2004; Freudenthal and Geiringer, 1958; Owen and Hinton, 1980]. In what follows we use the von Mises yield criterion which simply states that yielding occurs when $\sqrt{J'_2}$ reaches a certain critical value (or yield stress) k independent of stress and strain, so that the yield function $F(\sigma)$ writes:

$$F(\sigma) = \sqrt{J'_2} - k = 0 \quad (12)$$

In the Haigh-Westergaard (principal stress directions) space, this function defines a yield surface that is an infinite cylinder whose axis is given by $\sigma_1 = \sigma_2 = \sigma_3$.

2.2.5. Plastic Flow Rule

[21] In an isotropic material, the direction of the principal axes of stress and plastic strain rate must coincide: the Saint Venant-Lévy-Mises relation links the deviatoric stress tensor with the strain rate tensor through a constant λ . This condition is also sometimes referred to as condition of coaxiality and writes:

$$\dot{\epsilon} = \lambda s \quad (13)$$

Note that this equation is entirely similar to the equations of Newtonian fluids: $s = 2\mu\dot{\epsilon}$. The λ parameter plays the role of the inverse of an effective viscosity.

2.3. Two-Dimensional Punch Problem

[22] There are very few exact solutions to boundary value problems involving plastically deforming solids. Such solutions are usually either for highly simplified geometries (spherical or axial symmetry, for instance) or simplified material models (such as rigid plastic solids).

[23] The case of a rigid punch indenting a rigid plastic half space is one of them. The solution as shown on Figure 1

can be obtained by means of the slip line field theory, which gives exact solutions for plane strain boundary value problems. The plane strain formulation of the equations is presented in Appendix A and the detailed solution to the plane strain punch problem is derived in Appendix B.

3. DOUAR: A Nonlinear Fluid Solver

3.1. Background

[24] In the past few years, we have spent much effort developing a parallel 3-D finite element adaptive ALE code (named DOUAR) to study the deformation of slow nonlinear fluids [Braun *et al.*, 2008]. In problems involving certain nonlinear fluids, one expects to see regions of near zero measure with high velocity gradients. These regions will typically be surfaces (shear zones, faults) with a small transverse thickness in the direction of maximum strain rate.

[25] Since the plasticity theory that we use does not provide any length scale which can set the thickness of the shear zones, this thickness will be limited by the grid spacing. An accurate resolution of these shear zones will therefore require spatial discretization techniques capable of generating denser grids in these regions.

[26] Regular, nonadaptive grids would imply, for similar accuracy, prohibitive CPU time and memory requirements from the linear solver. The benefit of adaptive grids is much greater in 3-D than in 2-D due to the scaling of both these factors with the number of equations.

[27] DOUAR combines adaptivity and parallelism to overcome these limitations. It capitalizes on the recent development of parallel direct sparse solver such as PSPASES (Parallel Sparse Symmetric Direct Solver) (available at <http://www-users.cs.umn.edu/~mjoshi/pspases/>), WSMP (Watson Sparse Matrix Package) (available at <http://www-users.cs.umn.edu/~agupta/wsmp.html>) [Gupta, 2000], or MUMPS (Multifrontal Massively Parallel Sparse Direct Solver) (available at <http://graal.ens-lyon.fr/MUMPS>) [Amestoy *et al.*, 2000] and the increased availability of parallel platforms such as Beowulf clusters or multicore desktops.

[28] Even though DOUAR is a general nonlinear fluid ALE code, it was primarily designed to solve 3-D tectonic deformation problems, involving for instance continental collision or extension, as well as the formation of salt diapirs or the emplacement of granitic bodies. Over the past 20 years many numerical codes have been developed by the geophysical community around the plane strain (vertical cross section) [Fullsack, 1995] and plane stress (plan form, thin sheet) approximations [Houseman and England, 1993]. Plane strain approximation based codes are not capable of modeling strain-partitioning resulting from oblique convergence on a plate boundary and plane stress approximation provides a vertically integrated description of deformation and therefore cannot model the details of thrust and normal faulting.

[29] DOUAR is not limited by such hypothesis and solves the fully 3-D mechanical and thermal balance equations for nonlinear fluids. It uses Lagrangian particles to advect material boundaries and records Lagrangian quantities such as accumulated strain.

[30] The mechanical balance of slow viscous or viscoplastic fluids leads to a Stokes flow problem. For Newtonian fluids, the viscosity is a material parameter, while for viscoplastic fluids, the viscosity is an effective dynamical quantity which adjusts to the conditions to which the fluid is submitted. DOUAR solves a nonlinear form of the Stokes equation and we will focus in this article on the Eulerian computation of incompressible temperature-independent rigid plastic fluids.

[31] Such fluids are an idealization of real materials; they deform when stresses reach some given stress level: the yield stress. When stresses are below yield, the deformation rate is null. This model is useful for materials which will undergo elastic or viscous deformation below yield, small enough to be negligible by comparison to the plastic deformation accumulated on yield. This is typically the case for geological materials at low temperatures. (We can, to first order, neglect the change of volume resulting from the sustained deformation of rocks (this is, however, not valid for sedimentary rocks which are porous and can compact). Experiments indeed show that changes of volumes are restricted to the onset of deformation.)

3.2. Enforcing the Constraints

3.2.1. Incompressibility Condition

[32] In order to impose the incompressibility constraint, two widely used procedures are available, namely the Lagrange multiplier method and the penalty method [see Bathe, 1982; Hughes, 2000, and references therein]. It is the latter we have implemented in DOUAR.

[33] The basic step in the penalty formulation of viscous incompressible flow is the elimination of the pressure term in the equilibrium equations using

$$-\lambda \nabla \cdot \mathbf{v} = p \quad (14)$$

where λ is the penalty parameter, that can be interpreted (and has the same dimension) as a bulk viscosity. It is somewhat equivalent to say that the material is weakly compressible. It can be shown that if one chooses λ to be a relatively large number, the continuity equation $\nabla \cdot \mathbf{v} = 0$ will be approximately satisfied in the finite element solution. In the code, it is taken several (8) orders of magnitude larger than the shear viscosity μ .

3.2.2. Implementation of Plasticity

[34] The implemented method is an alternative to the radial return method proposed in many textbooks [Zienkiewicz and Taylor, 2002; Owen and Hinton, 1980]; instead of computing the normal to the yield surface in the principal stress space, and projecting any predicted stress state outside the surface onto this surface along the normal, one simply rescales the viscosity so that the point falls back on the surface.

[35] Practically, during the the FE matrix building process, the yield function F is computed in each element and for every Gauss-Legendre integration point, using the velocity solution obtained from the previous iteration:

$$F = \sqrt{J_2'} - k = 2\mu E_2' - k \quad (15)$$

where E_2' is the square root of the second invariant of the deviatoric strain rate tensor.

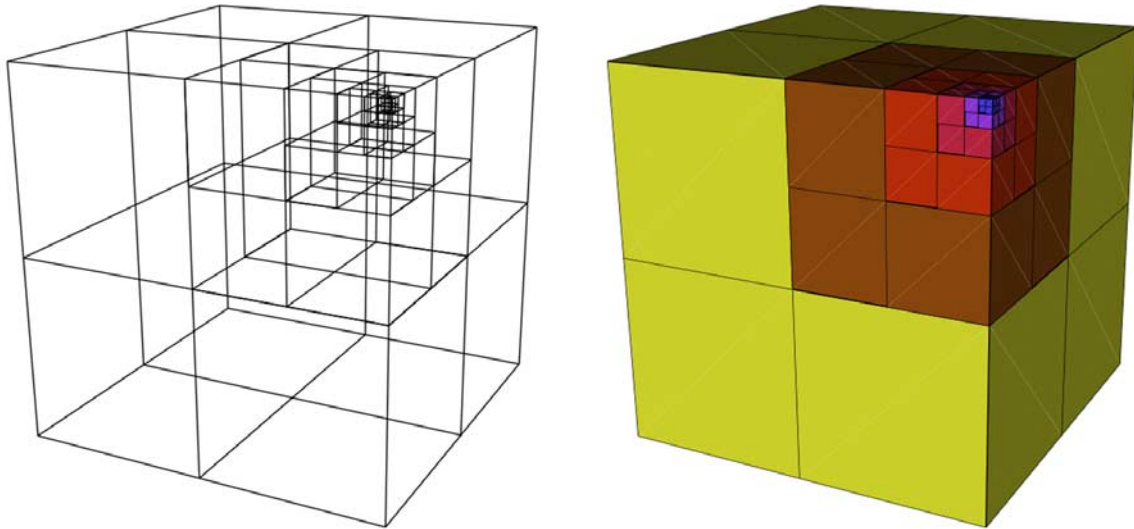


Figure 2. Example of a simple octree discretization of the unit cube. The unit cube is divided in eight subcubes, which can be arbitrarily divided into eight subsubcubes, and so on. The subcubes that remain undivided at the end of the construction of the octree are called leaves which are used here as finite elements with which the partial differential equations are solved.

[36] If $F > 0$ then the point under consideration is outside the yield surface, and by rescaling the viscosity to

$$\mu' = \frac{k}{2E_2'} \quad (16)$$

one insures that the nonlinear (plastic) relationship between strain rate and stress is respected. We refer to this method as the Viscosity Rescaling Method (VRM) [Kachanov, 2004; Willett, 1992].

3.3. Spatial Discretization

[37] One of the code's specificities is its reliance on an adaptive grid, built on octrees. An octree is a geometrical construct that divides three dimensional space in a space-filling set of cubes of varying size that are used here as basic trilinear eight-noded finite elements (Figure 2). Where cubes of different size share a common face, some of the nodes that are at the corners of the small elements do not exist in the adjacent large elements. These are called "bad faces" that are dealt with by imposing linear constraints.

[38] Octrees are very simple and memory-efficient entities that can be built as a single integer array containing, for each cube of the octree, the address in the array of the first of its eight "children cubes." When a cube is not divided, it becomes a leaf to which a name/number is associated and stored in the octree integer array as a negative number (to indicate that it corresponds to a leaf number and not a child's address).

[39] Octrees are very light and usually can be stored in a few kilobytes of memory. Furthermore, many operations commonly needed in the construction of a finite element problem are done with great efficiency on an octree, such as, for instance, the location of a point of known coordinates (i.e., to find the name/number of the leaf it belongs to), the determination of the size of all leaves/elements, finding the list of neighboring leaves/elements, the interpolation of a

field known at the nodes of an octree, or the union of two octrees.

[40] The unit cube is said to be of level zero as it only counts $(2^0)^3 = 1$ leaf. After one division, the octree has now $(2^1)^3 = 8$ leaves and is of level $L = 1$. Performing another subdivision of each leaf leads to a regular level $L = 2$ octree of $(2^2)^3 = 64$ leaves. Consequently a $32 \times 32 \times 32$ grid is a level 5 octree with 32,768 leaves.

3.4. Refinement Algorithm in Detail

[41] As mentioned earlier, one major drawback of uniform grid-based finite element codes is that in order to increase the accuracy, one must generate a denser grid, leading to rather large systems and hence long computational times, even though there probably are parts of the solving domain that do not require such a refinement. This limitation translates in the literature by 3-D grids that usually are of the order of $128^3 \simeq 2 \times 10^6$ elements for those which rely on square elements for instance.

[42] In the punch problem, only a small fraction of the total volume has a nonzero velocity, and this is in such a problem that local adaptive refinement shows its virtues. In the code, the octree (which also is the solving grid) is refined according to a criterion that the user may define. In what follows, this criterion is based on E_2' , the square root of the second invariant of the deviatoric strain-rate tensor $\dot{\epsilon}$.

[43] In practice, successive octrees are built and we use the velocity field known on a previous solve octree \mathcal{O}_{ps} corresponding to the last iteration to improve the resolution of the current solve octree \mathcal{O}_s : E_2' is measured for each leaf l of \mathcal{O}_{ps} , and we coin E_2^{\max} its maximum. Having defined a tolerance tol (typically of order a few percent), the center of each leaf l of \mathcal{O}_{ps} that verifies $E_2'(\dot{\epsilon}_l) \geq tol E_2^{\max}$ (criterion C_{ref}) defines a location in space where the solve octree \mathcal{O}_s is refined to a prescribed level L .

[44] The very specificity of our approach lies in the increasing level of grid refinement. The solve octree is first

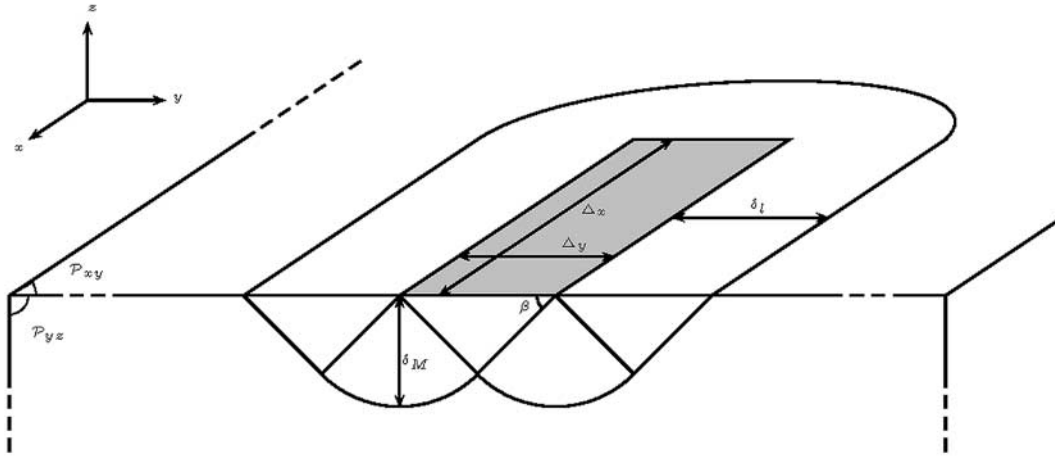


Figure 3. Experimental setup of the punch problem. The punch area is shown in grey color. The \mathcal{P}_{xy} plane corresponds to $z = 1$, and the \mathcal{P}_{yz} plane corresponds to $x = 1$. The lateral extent δ_l and the depth δ_M of the mechanism are indicated, as well as the angle β of the rigid wedge directly beneath the punch.

initialized at a uniform level L_u , which is typically taken equal to 5. According to the refinement criterion C_{ref} presented in the last paragraph, only a subset of leaves will be refined to a given level $L > L_u$. The value of L progressively increases one unit at a time to reach the authorized maximum level L_{max} . This increase takes place when both statements are true:

[45] (\mathcal{C}_1): for a given grid the nonlinear iterations performed on this grid have converged, i.e., the L_2 norm of the velocity field difference between two consecutive iterations k and $k + 1$ is less than a given input parameter η .

$$\frac{\|\{\mathbf{v}\}^{k+1} - \{\mathbf{v}\}^k\|_2}{\|\{\mathbf{v}\}^k\|_2} < \eta$$

[46] (\mathcal{C}_2): the refinement based on \mathcal{O}_{ps} has led to a solve octree \mathcal{O}_s whose number of leaves N_s is close or equal to the number of leaves N_{ps} of \mathcal{O}_{ps} , i.e.,

$$\left| \frac{N_s - N_{ps}}{(N_s + N_{ps})/2} \right| \leq \chi$$

where χ is a user supplied parameter.

[47] Schematically, the code structure is built upon three imbricated loops, as sketched on Figure 4. The outer loop (not shown) is the time stepping, the second one is the progressive adaptive grid construction, and the inner third one is the nonlinear iterations one.

4. Numerical Experiments

4.1. Problem Setup

[48] In this section we describe the numerical experiments we have performed. One of the faces of the simulation domain (unit cube) is “punched” by a rectangular surface of aspect ratio R . The two end-members of these simulations are $R = \infty$ and $R = 1$. The first case corresponds to an

infinitely long punch, which is a way to perform plane strain experiments (the same two-dimensional problem is repeated infinitely in the third direction). The solution to this problem is given in section 2 and derived in Appendix B. It has been extensively studied numerically [Zienkiewicz *et al.*, 1995; Christiansen and Pedersen, 2001; Christiansen and Andersen, 1999; Huh *et al.*, 1999; Yu and Tin-Loi, 2006]. The second case is a three-dimensional square punch problem to which no analytical solution exists but which has been investigated numerically in the framework of bearing capacities studies [Gourvenec *et al.*, 2006]. In what follows, we not only investigate these two cases but also intermediate values of the aspect ratio R .

[49] The geometry of the simulation setup is shown on Figure 3. The unit cube is filled with a single material of known von Mises yield stress k . We apply a given velocity w_p on a rectangular region of size $\Delta x \times \Delta y$ of the face $z = 1$. In order to simulate a two-dimensional punch, we simply replicate the experiment in the x direction, i.e., $\Delta x = 1$. On the bottom of the cube, as well as on the two faces $y = 0$ and $y = 1$ zero velocity boundary conditions are imposed, while on the two faces $x = 0$ and $x = 1$ only the normal velocity component u is set to zero.

[50] This is a single timestep problem, and the parameters common to all simulations are given in Table 1. All

Table 1. Parameters Used in All the Simulations

Parameter	Value
Yield stress k	1
Viscosity μ	10^4
Bulk viscosity λ	$10^8 \mu$
Punch width Δy	0.08
Uniform octree level L_u	5
Maximum octree level L_{max}	8
Imposed punch velocity w_p	1.05
Velocity convergence tolerance η	0.001
Octree convergence tolerance χ	0
Gravitational acceleration g	0

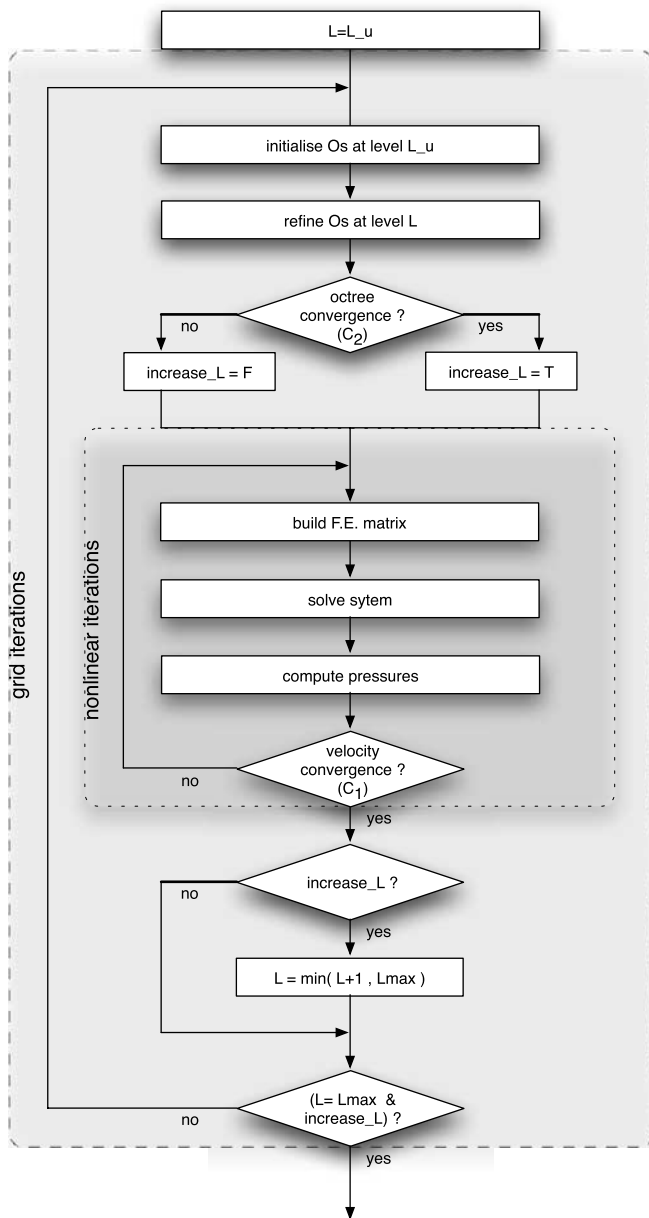


Figure 4. Schematic overview of the grid construction and nonlinear iterations nested loops within one time step of DOUAR.

simulations were run on our 16 node cluster, each node being a biprocessor dual core 2.2 GHz Operon box. The nodes are connected by the InfiniPath interconnect.

4.2. Reference Case

[51] Knowing the analytical solution to the two-dimensional problem certainly is a great asset in order to assess the performance of the code. In order to better appreciate the effect of using a highly irregular grid on the solution and evaluate its accuracy, one would want to calculate the solution on a maximum level regular grid. This is unfortunately impossible in three dimensions: the size of a level 8 uniform ($256 \times 256 \times 256$) three-dimensional octree based finite element grid is clearly beyond the computational ability of our cluster.

[52] Consequently, we have devised the following reference numerical experiment: in theory, if the code was able to resolve all the slip lines (repeated in the third dimension) exactly, the octree on which the computations are based should only be refined along these lines, and this octree should constitute a reference discretization. We have analytically built such an octree (see Figure 5a) and carried out computations on it. In total, this grid counts 142,080 leaves/elements and 501,924 degrees of freedom.

[53] One of the aims of the following computation is to demonstrate that our dynamic meshing algorithm converges toward a spatial discretization that is optimized for the problem at hand, or more exactly its solution. On Figures 5b, 5c, and 5d are shown the computed velocity field, its norm, and the E_2' field, respectively. One sees that the code converges toward the correct expected solution in terms of slip lines and velocity field.

[54] On Figure 6a is plotted the L_2 norm of the velocity field difference between two successive nonlinear iterations as a function of nonlinear iterations (it is this value that is used in criterion C_1 and compared to η). One sees that after 150 nonlinear iterations, the velocity field computed on the grid has converged and stabilizes at its final value (around $7. \times 10^{-4}$).

[55] Figure 6b shows the minimum of the computed elemental E_2' field. Since the analytical solution involves rigid blocs in rotation and translation, the strain rate (and consequently E_2') should be null in these regions. One sees that after 1000 nonlinear iterations, the minimum of E_2' we obtain is 6.8×10^{-2} (the maximum $E_2'^{\max}$ being 109.3). In the rigidly rotating regions, the remnant E_2' field is approximately 11.4% of $E_2'^{\max}$ which corresponds to a residual velocity field in the blocs of 0.7% of the imposed punch velocity.

[56] One should notice that even though this reference grid appears to be idealistic in terms of refinement, it is also very irregular: in a rather very narrow space, there exists a juxtaposition of leaves of various levels, a fact which is known to introduce numerical artifacts due to the linear constraints on bad faces. In the following subsection we present the solution obtained with the adaptive grid method and compare it with this one.

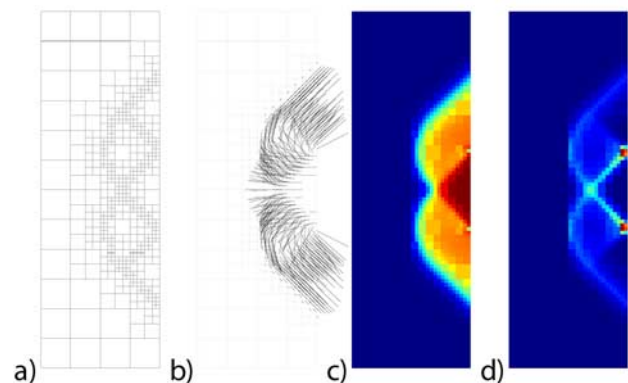


Figure 5. Closeups of the reference octree cross sections taken at $x = .5$. (a) Grid, (b) velocity vector, (c) velocity field, and (d) E_2' field. Blue color indicates low values and red color indicates high values.

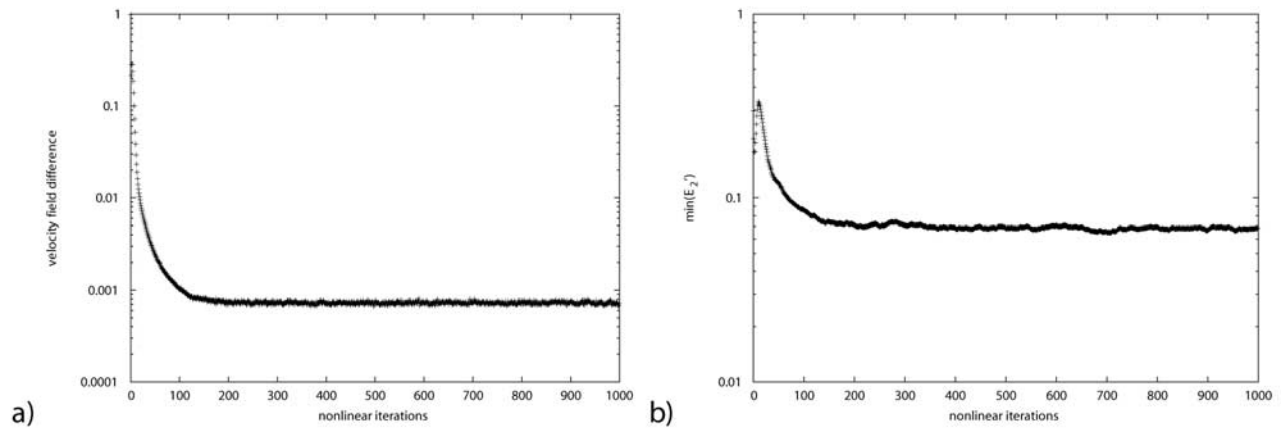


Figure 6. On the reference grid: (a) measure of the velocity field difference between two successive nonlinear iterations as a function of the nonlinear iterations; (b) measure of the minimum of E_2' field within the mechanism as a function of nonlinear iterations.

4.3. Plane Strain Limit

[57] In this section, we now make full use of the ability of the code to progressively refine the finite element grid accordingly to the criterion presented in section 3.4, and compare the results with those obtained on the reference grid previously shown.

[58] All simulation parameters are those of Table 1. In total, the code generates and uses 13 grids to produce a velocity field solution that complies with the convergence criteria C_1 and C_2 . The first two are of uniform level 5, the next four are of level 6, the next three are of level 7, and the final four are of level 8.

[59] When the code generates for the first time a grid at a higher level than the previous one, around 40 nonlinear iterations are necessary in order to reach velocity convergence, while when the code successively produces “better” grids at a given level, the number of nonlinear iterations remains between 1 and 5.

[60] On Figure 7 are presented close-ups ($x = 0.5, 0.3 \leq y \leq 0.7, z \geq 0.8$) of cross sections of the 1st, 3rd, 6th, 7th, 9th, 10th and 13th grids. Figure 7a is then a portion of the initial uniform grid, Figures 7b and 7c correspond to the first and last grids generated at level 6, Figures 7d and 7e correspond to the first and last grids generated at level 7, and Figures 7g and 7h correspond to the first and last grids generated at level 8.

[61] On the initial grid, nonlinear iterations are carried out, until the velocity field complies with criterion C_1 . Since no previous octree exists, the C_2 criterion fails, and therefore no increase of level is performed. On the second grid, still of uniform level 5, only one nonlinear iteration is necessary to reach convergence, and this time the C_2 criterion is verified.

[62] At that time, both criteria C_1 and C_2 are true, so the velocity field (or rather E_2') is used to refine elements where this field is larger than tol times its maximum on all leaves. The resulting grid is shown on Figure 7c. The solution is then computed on this grid and used to create a new grid. As long as the C_2 criterion is not satisfied, the code iterates this process, until an increase of level can take place, up to level 7, then 8. The last generated grid is the one at maximum level L_{max} on which both criteria C_1 and C_2 have been found true.

[63] If we now compare Figure 5a with Figure 7h, we see that the code does not naturally converge toward the optimum or reference grid. This was, however, to be expected since the reference grid is based on an analytical solution that incorporates discontinuous velocity fields, and infinitely thin slip lines, features that are not attainable for our type of formulation: the computed velocity field is continuous, and the shear zones “thickness” is limited by the size of the smallest element. On the other hand, if one was to use a different refinement criterion such as velocity

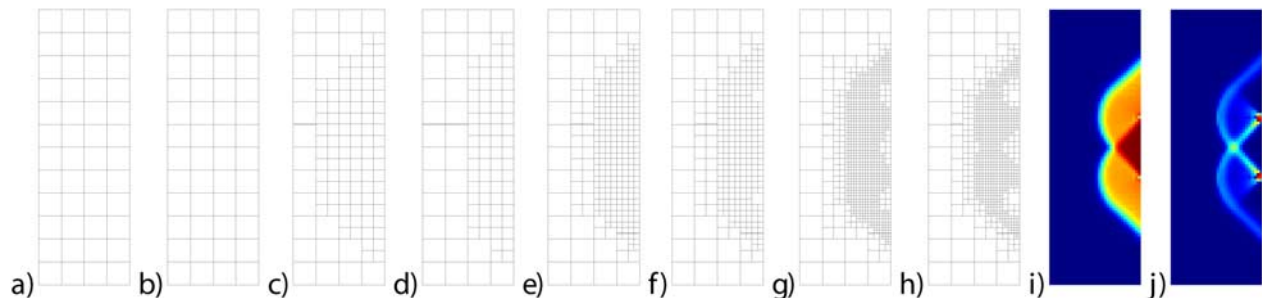


Figure 7. Closeups of octree cross sections ($x = 0.5$) for the plane-strain experiment. (a–h) Succession of generated grids; (i) velocity norm field; (j) E_2' field.

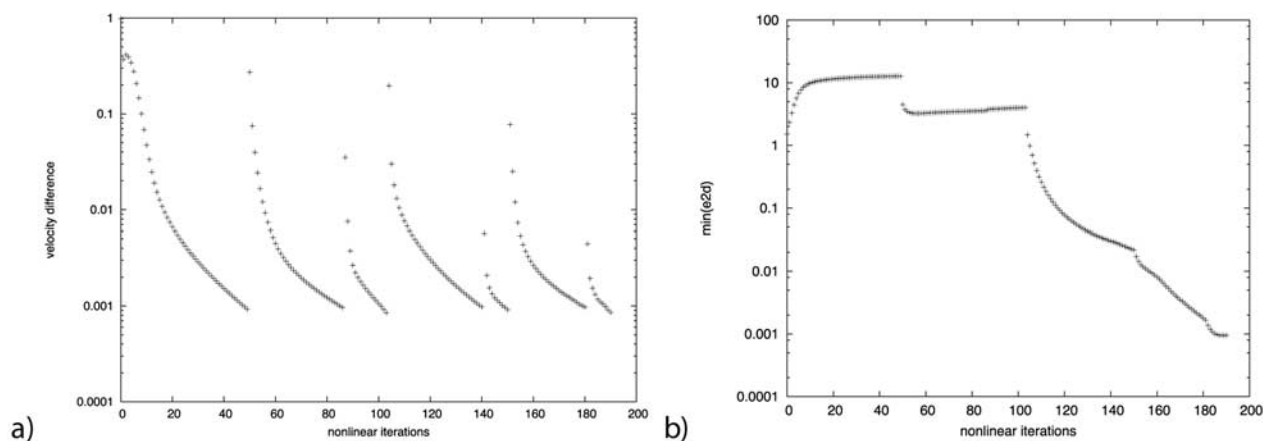


Figure 8. On the successive generated grids: (a) measure of the velocity field difference between two successive nonlinear iterations as a function of the nonlinear iterations; (b) measure of the minimum of E_2' field within the mechanism as a function of nonlinear iterations.

field curvature, it would be possible to produce less refinement in the rigid zones (see <http://129.173.105.106/mort-PhilippeFullsack/qute2007.html> for instance).

[64] Bearing this in mind, the computed grid resembles, however, the reference one, except for the two regions of rigid rotation. The E_2' field in these regions appears to always remain slightly higher than in the three rigid wedges that translate as unrefined regions on the grid. In this case, the remnant E_2' in these regions is only 9.1% of $E_2^{\max} = 101.7$ which leads to a residual velocity field of 0.6% of the imposed velocity punch. The capture of the slip lines requires twice as many elements across than needed on the reference case. Even though one might be tempted to say the computed grid is not satisfactory, the fact that it contains (too) many high level elements allows for the velocity solution to be much smoother than on the reference grid (compare Figure 7i and 5c).

[65] Figures 8a and 8b are to be compared with Figures 6a and 6b respectively. We see on Figure 8a the effect of the successive production of grids. For every new grid, and because the velocity field is interpolated from a previous grid onto a new one, this process throws back the velocity convergence value some two orders of magnitude back up, i.e., the system is sent out of static and plastic equilibrium when a new grid is generated. In total, the code performs 191 nonlinear iterations spread onto the 13 grids, and on each of the grids it reaches the convergence value $\eta = 0.001$.

[66] More importantly, the minimum of E_2' within the mechanism reaches its lowest value (around 10^{-3} with a maximum E_2^{\max} of 101.7) on the last grid (Figure 8b). This value is one order of magnitude smaller than in the reference case. It is explained by a more regular grid, hereby ensuring a smoother solution, and hence a better accuracy and a better capture of rigid block motion. Finally, the plot (Figure 8b) can be split in four parts, each one of them corresponding to one of the four successive refinement levels. Every time the level is increased, the minimum value of E_2' reaches a lower value in the rigid wedges.

[67] In Appendix B, we derive the analytical form of σ_{zz} beneath the punch. This analytical value is compared with the measurements performed on the reference grid and on

the (last) generated grid in the plain strain case. Numerically, the value of σ_{zz} is calculated as follows: first, we compute the nodal reaction forces $\mathbf{f} = (f_x, f_y, f_z)$. Then, we find the leaves that are completely under (and in contact with) the punch, and average the four f_z values of the nodes given by $z = 1$ for each of these leaves. We divide this elemental f_z force by the leaf area, and obtain σ_{zz} for each leaf under consideration. We also compute another quantity $\langle \sigma_{zz} \rangle$, calculated by summing all the f_z values at the nodes touching the punch and dividing this sum by the punch area.

[68] On Figure 9 are plotted the elemental measurements σ_{zz} and their average $\langle \sigma_{zz} \rangle$ for both experiments. The theoretical constant value $\sigma_{zz}^{\text{th}} = -k(2 + \pi)$ is shown for reference. We see that the reference run, again because of the coarseness of the grid leads to values approximately 30% higher than the theoretical value on average while the average value measured on the generated grid overestimates this value by less than 3%. Also, an undershoot/overshoot of pressure is observed at the edges of the punch as pressure there is singular. If the resolution was increased, the edge

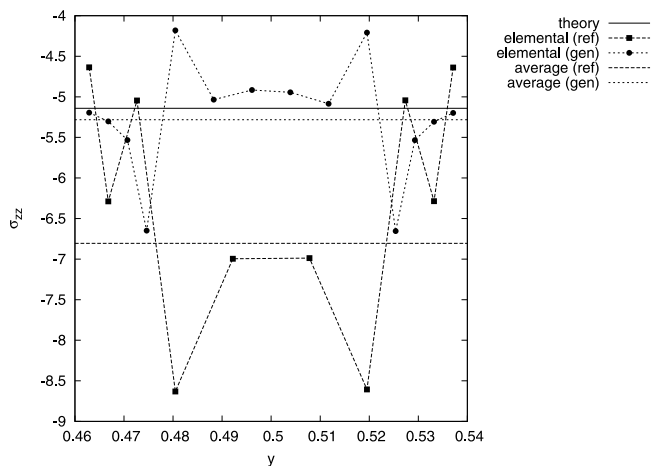


Figure 9. σ_{zz} measurements directly beneath the punch on the reference grid and on the last generated grid for the plane strain experiments.

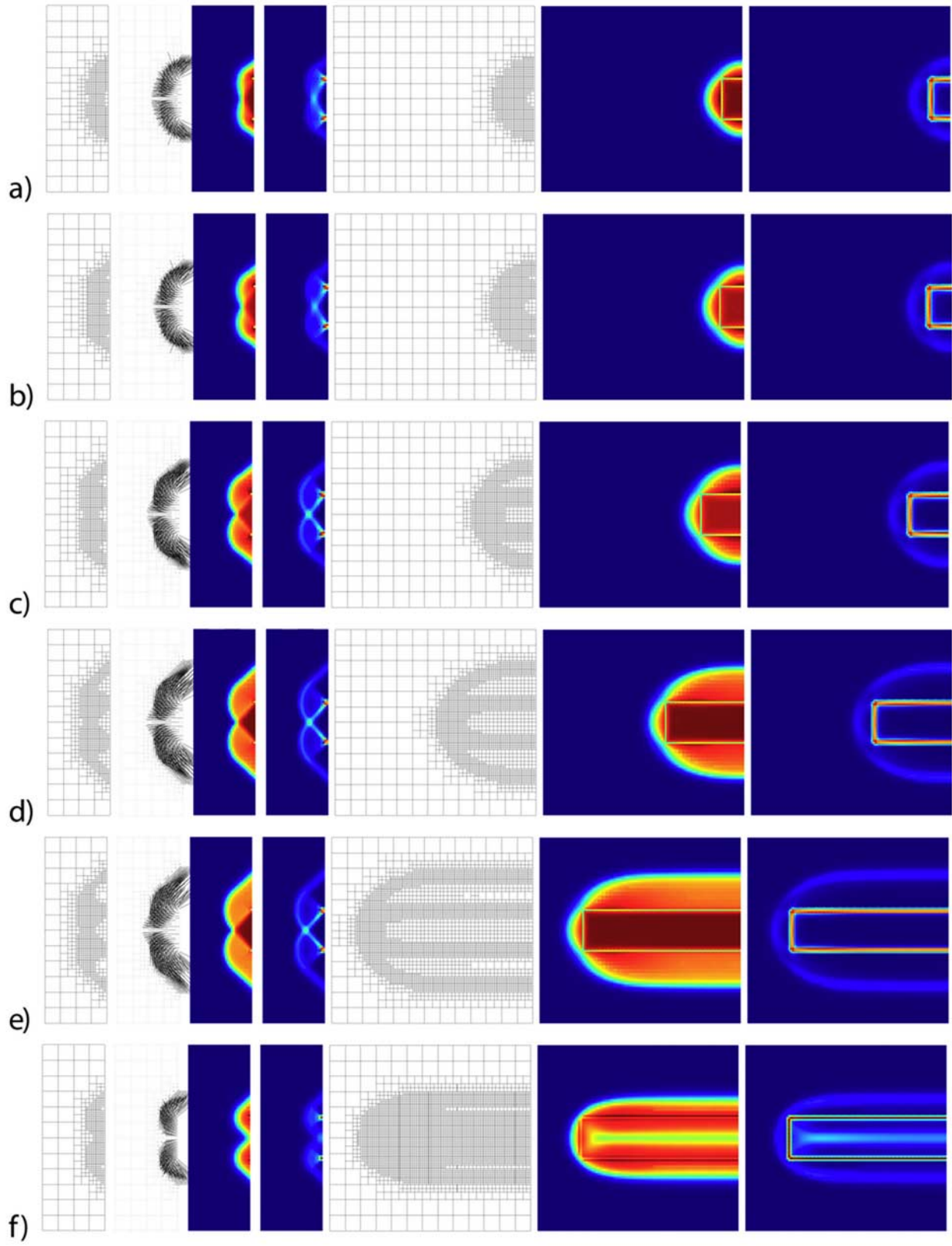


Figure 10. Planar zones of influence of the failure mechanisms (see text for legend).

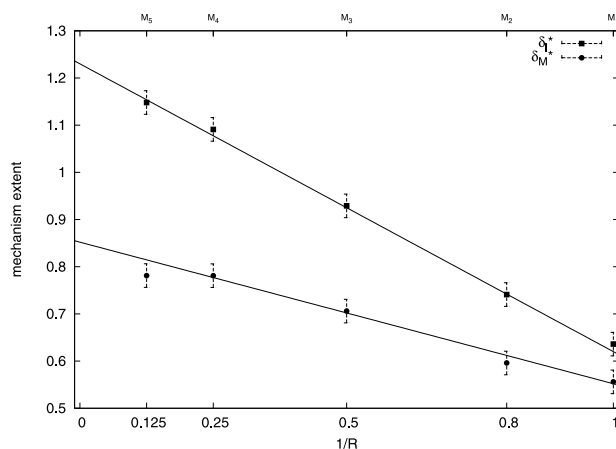


Figure 11. Extent of failure mechanism as function of the inverse of the punch aspect ratio for rough boundary conditions.

effect could be confined within a few elements of the edges, and this would improve the stress measurements. Finally, in the middle part of the punch, the computed stress by our method is a lower bound as observed on Figure 9.

[69] Our results, while being acceptable, are not exceptional: it should be realized that in two dimensions, the limit load of Prandtl’s problem can be obtained within a few percents or less [Yu and Tin-Loi, 2006; Christiansen and Pedersen, 2001; Lyamin and Sloan, 2002] with numerical methods that could easily be implemented in 3-D.

4.4. Rectangular Punch

[70] The previous numerical experiments were carried out within the plane strain approximation. While DOUAR has shown its ability to capture adequately the expected analytical solution, a similar two-dimensional quadtree based Q1-P0 finite element code would have sufficed, and would have certainly required far less memory and CPU time for the same accuracy.

[71] If one now considers a punch of finite length ($\Delta x < 1$), then the three-dimensional nature of our code becomes a key feature to study the mechanism of a rectangular punch indenting a rigid plastic space. A series of three-dimensional models were run to investigate the effect of varying the length to breadth aspect ratio of the strip. Looking at the geometrical setup of our simulations (Figure 3), we see that only half of the strip is actually accounted for in the simulation, so that the aspect ratio R of the strip is given by $R = 2\Delta x/\Delta y$.

[72] Another distinction between models can also be made: when u and v velocity components are left free (which mimics a frictionless interface between the punch and the material) then one speaks of a smooth punch, as opposed to a rough one when these components are fixed to zero. We have chosen five geometrically different models with $\Delta y = 0.08$ and different Δx : model M_1 ($\Delta x = 0.04, R = 1$), model M_2 ($\Delta x = 0.05, R = 1.25$), model M_3 ($\Delta x = 0.08, R = 2$), model M_4 ($\Delta x = 0.16, R = 4$), model M_5 ($\Delta x = 0.32, R = 8$),

[73] On Figure 10 are shown (from left to right) (1) four cross sections of the octree, of the velocity field, of the velocity norm field, and of the E_2' field in the plane \mathcal{P}_{xy} ($x =$

$0, 0.3 \leq y \leq 0.7, z \geq 0.8$), (2) three cross sections of the octree, of the velocity norm field, and of the E_2' field in the plane \mathcal{P}_{yz} ($x \leq 0.4, 0.3 \leq y \leq 0.7, z = 1$), for the M_1 (rough), M_2 (rough), M_3 (rough), M_4 (rough), M_5 (rough) and M_5 (smooth) experiments, from top to bottom.

[74] Experiment M_1 of unit aspect ratio corresponds to the smallest value of the aspect ratio for a rectangular punch, and therefore constitutes a typical fully three-dimensional problem. When the aspect ratio increases, the setup then resembles more and more a two-dimensional one except near the end of the strip.

[75] Looking at Figures 10a–10e, the following observations can be made:

[76] 1. The M_1 model corresponds to a square punch. The grid, as well as the measured fields show a fourfold symmetry, as expected from the symmetry of the problem.

[77] 2. With increasing aspect ratio R , the depth and lateral extent of the resulting deformation increase, and finally reach the values obtained for plane strain experiments (valid for both rough and smooth experiments).

[78] 3. The angle β (see Figure 3) beneath the punch takes values ranging from approximately 23° ($R = 1$) to 45° ($R = 8$), as observed by Gourvenec et al. [2006].

[79] 4. It can be postulated that the plane strain conditions seem to be valid up to around $2\Delta y$ from the end of the strip.

[80] 5. With increasing R , the regions in which the plane strain approximation holds allow the code to better capture the regions of rigidly moving blocks. This visually translates into nonuniformly refined grids in moving regions (when an element is rigid, its strain rate is very small and therefore does not require further refinement of the element).

[81] Comparing now Figures 10e and 10f, i.e., results of geometrically similar experiments that only differ by the type of imposed velocity boundary conditions under the punch (rough versus smooth), one sees that the solutions are quite different. Looking at the E_2' field, it appears that using rough boundary conditions leads to a Prandtl type of solution (see Figure 1a), while smooth boundary conditions lead to a Hill type of solution (see Figure 1b). In the smooth case, since slip is possible under the punch surface, no

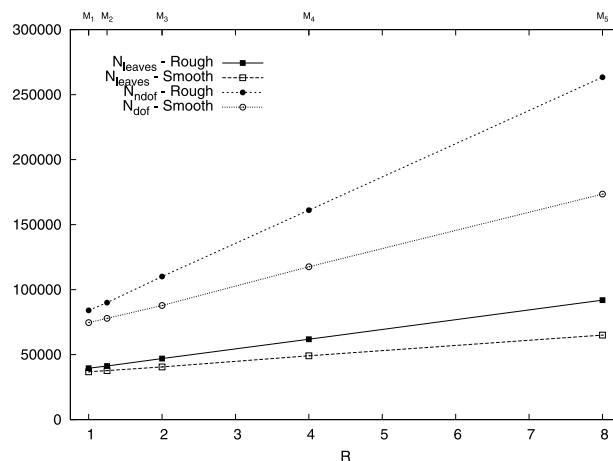


Figure 12. Number of leaves and degrees of freedom as a function of the aspect ratio R .

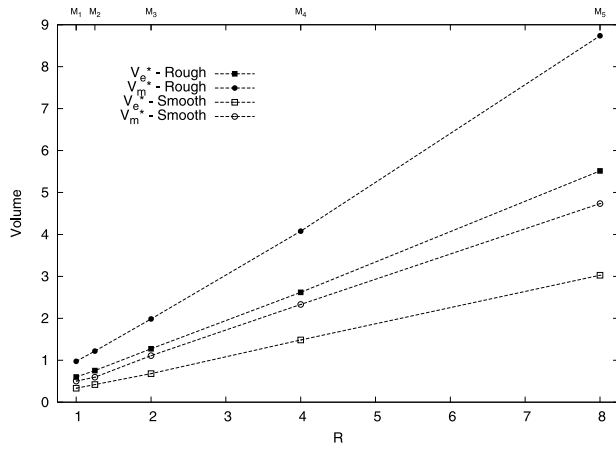


Figure 13. Volume V_m and slip volume V_e as a function of the aspect ratio R .

unique rigid wedge develops as observed in the rough case, but two smaller ones are present, centered on the extremities of the punch lateral extent. This translates into a much shallower deformation pattern, and a more uniform grid to capture it.

[82] In order to measure the extent of the deformation pattern, we look now at the zone of influence of the failure mechanism characterized by its maximum depth $\delta_M^* = \delta_M / \Delta y$ value and its lateral extent $\delta_l^* = \delta_l / \Delta y$ value. As observed by *Gourvenec et al.* [2006] both values linearly scale with the inverse of the aspect ratio (Figure 11).

[83] If we now look at the number of elements and the number of degrees of freedom (two indicators of the size of the problem the solver is faced with) we see that both increase linearly with the aspect ratio R (see Figure 12). Values obtained for rough punches are always larger than those obtained for smooth ones, due to a deeper mechanism. When R increases, it simply increases the volume of the mechanism (of constant section) linearly with it, and the grid size scales linearly with it too. The volume V_m is measured as the sum of the volumes of the elements whose average velocity is larger than 1% of w_p and the linear relationship between the dimensionless volume $V_m^* = V_m / \Delta y^3$ with R is shown on Figure 13.

[84] We have also measured the total volume V_e of the elements in which criterion C_{ref} is true, i.e. high strain rate elements that we can interpret as shear zones. Its dimensionless counterpart $V_e^* = V_e / \Delta y^3$ also scales linearly with the aspect ratio (Figure 13). We could also divide V_e by the

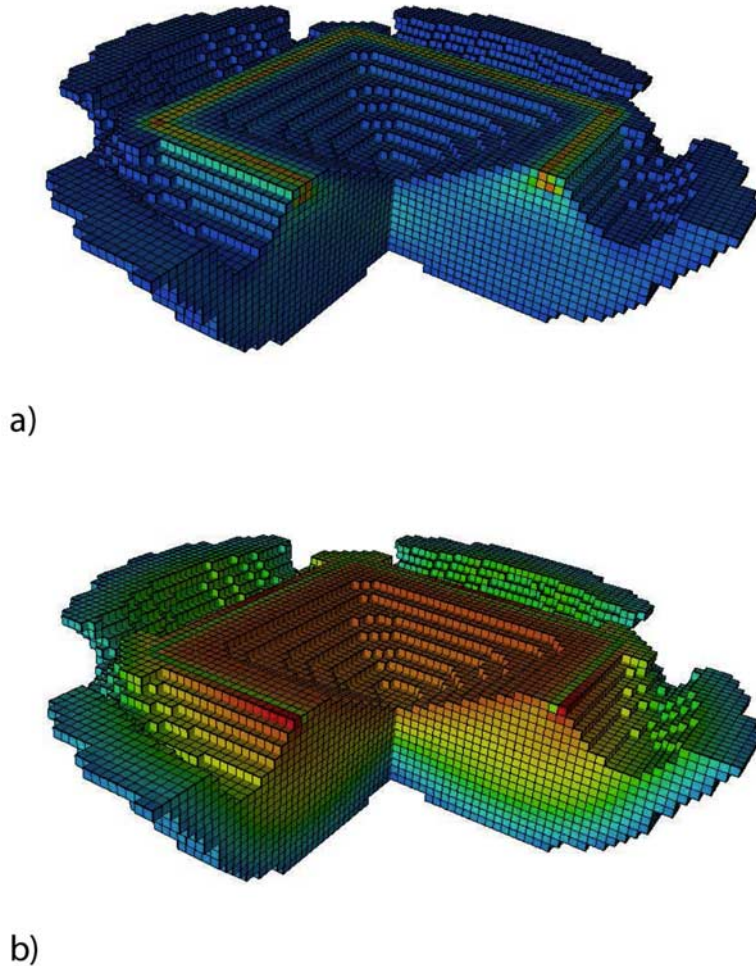


Figure 14. Subset of the elements that verify criterion C_{ref} of the last generated grid in the case of the central square punch. (a) E_2' field; (b) velocity norm field.

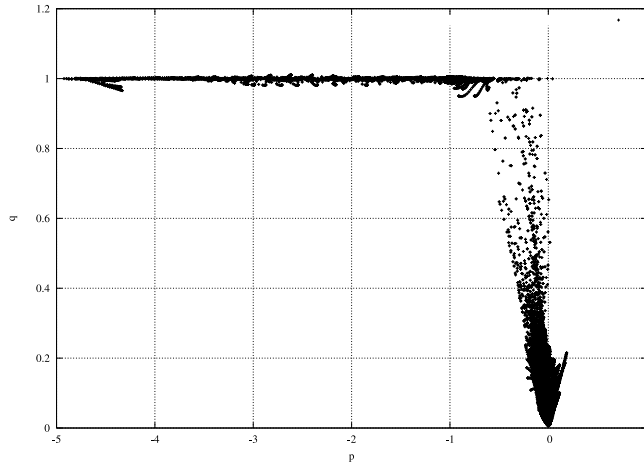


Figure 15. The qp -gram corresponding to the solution of the plane strain experiment. The quantity $q = 2\mu'E_2'$ shows an upper bound which is the yield stress $k = 1$ of the material.

‘thickness’ of the shear zones (i.e., the size of the elements of level L_{\max} that represent them) and therefore obtain a quantity homogeneous to a surface, which could be interpreted as the total shear zones surface S_e .

[85] Finally, in order to illustrate the mechanism of the square punch, we have carried out a simulation where the punch, of size 0.15, is centered on the $z = 1$ face of the unit cube, all other parameters being kept as in Table 1. On Figure 14 are only shown the elements that verify $E_2' \geq \text{tol} \times E_2^{\max}$ and which are not in the region of space ($x > 0.5$; $y > 0.5$). On Figure 14a the elements are colored by their E_2' value, while on Figure 14b they are colored by their average velocity. By doing so, we can get an insight on how the rigid parts are laid in three dimensions (they appear as excavated on the figures due to very low values of E_2'). As already observed on the cross sections, we see the presence of a central pyramidal shaped rigid wedge, bordered by four regions on each side of the square. An even higher level grid might allow for a better capture of what happens at the corners, and how the shear zones connect.

5. Discussion

5.1. Pressure Measurements and Smoothing

[86] In finite element terminology, the type of elements used is called $Q1-P0$ [Bathe, 1982], which implies that the velocity field is continuous but the pressure field is not. The elemental pressure is simply obtained by computing the divergence of the velocity field within each element and by multiplying it by the penalty factor λ (see equation (14)).

[87] However, this type of element is affected by a spurious element-by-element checkerboard mode [Bathe, 1982; Hughes, 2000] and the introduction of the linear constraints into the set of finite element equations further enhances these unwanted oscillations. Various methods have been used to improve the accuracy of pressures. Some are based on implicit stabilization, others are based on postprocessing of the solution, such as least squares fitting [Hughes, 2000; Zienkiewicz and Taylor, 2002]. We have resorted to a smoothing operation that needs to be per-

formed in our case so that the pressure field becomes usable in a pressure-dependent yield criteria, for instance.

[88] The algorithm implemented in our code is simple and is standard practice in the CFD community [Bochev et al., 2006]. The pressure is smoothed by performing a double interpolation of the elemental pressure onto nodes and then back onto elements.

[89] The element-to-node interpolation is performed by averaging the elemental values from elements common to each node; the node-to-element interpolation is performed by averaging the nodal values element-by-element. This method is not only very efficient but produces a smoothing of the pressure that is adapted to the local density of the octree. Note that these two steps can be repeated until a satisfying level of smoothness (and diffusion) of the pressure field is attained.

[90] On Figures 18a and 18b are shown the pressure field before and after smoothing, in the case of the M5 (rough) model. One sees that the checkerboard mode has indeed disappeared. Pressure measurements right beneath the punch were carried out and compared to the expected analytical value and were found to fall within a few percents of this value.

5.2. Satisfaction of Constraints

[91] In this work we are primarily concerned with the enforcement of the constraints (incompressibility and rigid plasticity) in order to simulate as closely as possible the ideal case of the two- and three-dimensional punch problem. We shall discuss hereafter the code behavior with regards to these issues.

5.2.1. Incompressibility

[92] The penalty formulation, controlled by the bulk viscosity, ensures in a nonexact manner (as opposed to the Uzawa algorithm [Arrow et al., 1968; Benzi et al., 2005]) the incompressibility of the material. For every grid generated and for every nonlinear iteration, the divergence of the velocity field on all elements has been recorded. The measurements are of the order of 10^{-12} – 10^{-13} and are to be related to the precision of the machine and roundoff errors.

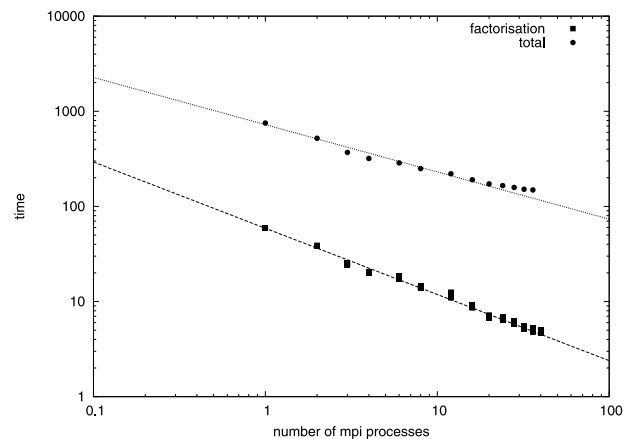


Figure 16. Average factorization time of the matrix and total run time as a function of the number of MPI processes for a reference run of 10 nonlinear iterations on a unique grid of 55168 elements.

Table 2. DOUAR Performances for the Square Punch Problem: Comparison Between the Uniform and the Adaptive Grid Approaches

	Uniform Grid	Adaptive Grid
Number of used grids	1	20
Total number of nonlinear iterations	40	116
Total run time	1456 s	810 s
Total (factorization + back-substitution) time	1351 s	576 s
Number of leaves	168,092	32,768 → 84,589
Number of nodes	181,557	35,937 → 95,288
Matrix size	485,865	49,005 → 227,058
Number of nonzero terms	20,768,181	1,845,144 → 10,142,334
Real workspace needed by the solver	10.8 Gb	0.8 Gb → 6 Gb
Average factorization time	33 s	1 s → 10 s
Average back-substitution time	0.57 s	0.07 s → 0.26 s
(Factorization + back-substitution time)/(total time)	93%	71%

5.2.2. Rigid Plasticity

[93] The rigid plasticity model implies that (1) stresses reached in the material cannot exceed the yield value k and (2) the deformation is null where stresses are below the yield value.

[94] The first hypothesis is checked by plotting what we have coined a J-gram: it is a plot of all spatial samples of a tensor field in the space of its invariants. More particularly, it is a qp -gram since we represent $q = 2\mu'E_2'$ as a function of the pressure p . On Figure 15 is shown such a qp -gram for the plane strain simulation. One sees that the VRM algorithm, which applies repeated rescaling of the viscosity (therefore driving the stresses inside or close to the yield envelope) leads to a plot where some of the sample points are indeed located very close to the maximum value $k = 1$ while all the others remain below the yield value. By decreasing the convergence parameter η , we manage to progressively bring back elements with $q \geq k$ closer to the yield value k .

[95] The second hypothesis has been confirmed by the simulation. Regions that move as rigid blocks translate into coarse grid regions.

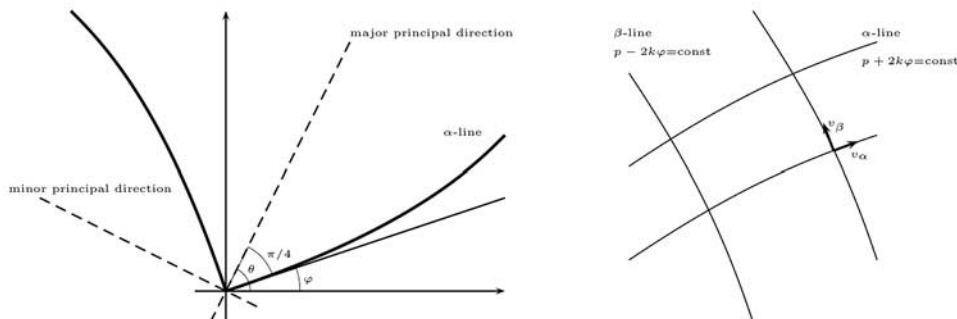
5.3. Efficiency

[96] The code is almost fully parallelized by means of the MPI paradigm [Braun et al., 2008] and in order to illustrate this, we have carried out the same simulation with different number of MPI threads (from 1 to 36). Each of these simulations consisted of 10 nonlinear iterations on a 55,168 elements and 139,557 degrees of freedom grid. If the code and the solver scaled perfectly with the number of MPI threads, we would expect their respective timings t_s

and t_c to be proportional to the inverse number of processes n , i.e., $t \propto n^\alpha$ with $\alpha = -1$. On a log-log plot, this would translate as a line of -1 slope. In order to characterize the scaling performances of the solver and the code, we measure the slope of the measured times t_s (averaged over the 10 iterations) and t_c as a function of $1/n$ on a log-log plot, see Figure 16. A least squares fit leads to a scaling of the solver proportional to $n^{-0.7}$ while the scaling of the code is proportional to $n^{-0.5}$.

[97] The efficiency of our adaptive code, as well as the justification for the use of the grid refinement algorithm, can be assessed by means of a simple comparison between two experiments. The square punch experiment was run again on 32 MPI processes with the same parameters as in section 4.4, but a uniformly refined grid at level 8 was generated in a region large enough to contain the observed solution in the adaptive case. In this case, only one grid is used and once the nonlinear iterations have converged (criterion C_1 is true), the run ends since the criterion C_2 is automatically verified.

[98] All other things equal, various data concerning each experiment are shown in Table 2. In both cases it is important to note that the time devoted to the solver takes between 70% and 90% of the run time. However, it is obvious that in order to obtain the same solution with the same precision, the adaptive strategy is more advantageous. First, it runs faster: indeed, even though 116 nonlinear iterations are necessary, 88 of them are performed on grids at uniform level 5, 6, and 7 and each of them takes less than 2 s. This results in a total time spent in the solver being about half the one spent in the regular grid case. Then, because the adaptive algorithm produces smaller grids, less memory is required by the direct solver to solve the system.

**Figure 17.** Principal directions of stress and slip lines.

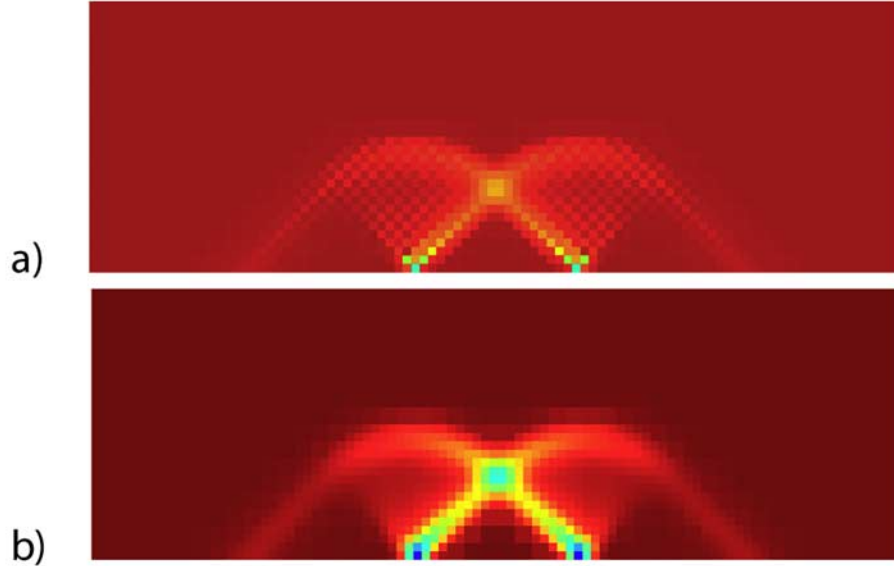


Figure 18. Closeup of the pressure field (a) before and (b) after smoothing in the plane strain experiment. Red color indicates regions of zero values; blue colors indicate regions of maximum values.

Since the amount of memory available per CPU is limited, this approach might allow to carry out computations to a given precision that would normally not fit on a given machine with a uniform grid approach. Finally, if one was to set L_{\max} to 9, this difference in terms of overall performance between the two approaches would be further increased as the adaptive grid run would take the same steps as in the $L_{\max} = 8$ case before carrying on with $L = 9$ grids, while the uniform grid run would have performed all its nonlinear iterations on a very large grid.

5.4. Frictional (Pressure-Dependent) Plasticity

[99] As previously stated, the Mohr-Coulomb criterion is commonly used to represent the frictional behavior of rocks and unlike the von Mises criterion requires two rheological parameters, the dimensionless angle of friction ϕ and the cohesion c that has units of pressure:

$$\tau = c - \sigma_n \tan \phi \quad (17)$$

where τ is the magnitude of the shearing stress and σ_n is the normal stress. This criterion corresponds to an hexagonal pyramid in the principal stress space. Under some circumstances or in different materials, this pressure dependence can be neglected and the criterion is simplified to become the von Mises criterion that we have used all through this paper. However, under Earth-like conditions, the frictional behavior becomes dominant.

[100] An approximation to the Mohr-Coulomb law was presented by *Drucker and Prager* [1952] as a modification of the von Mises yield criterion. An additional term in the von Mises expression is added to take in account the influence of the hydrostatic stress component on yielding:

$$F(\sigma) = \sqrt{J_2} - \alpha p - k = 0 \quad (18)$$

This yield surface has the form of a circular cone, and the coefficients α and k can be chosen as functions of the cohesion c and angle of friction ϕ in order to make the Drucker-Prager circle coincide with the inner or outer apices of the Mohr-Coulomb hexagon at any section [*Owen and Hinton*, 1980].

[101] In order to show the code's capability to deal with a material characterized by a pressure-dependent yield criterion in the presence of a gravity field, we have performed a lateral punch experiment: a velocity $-v_p$ is applied onto nodes i with $y_i = 1$ and $0.45 \leq x_i \leq 0.55$. All parameters are still those of Table 1 but in this particular case $\rho g = 10$, with the gravity acceleration vector pointing downwards. The parameters of the Drucker-Prager criterion are $k = 1$ and $\alpha = 0.25$. On the punched face, only the nodes under the punch area have a fixed velocity, while on all other faces, no outward flow boundary conditions prevail.

[102] On Figure 19 are shown the results of this simulation: we show on Figures 19a, 19b, and 19c the whole cube (the computational domain) and the emplacement of the lateral punch is clearly visible. We observe that the velocity $|\mathbf{v}|$ field, the E_2' field and the smoothed pressure field vary with z and are of three-dimensional nature.

[103] In order to better visualize these variations, we present cross sections of the cube in four planes: $x = 0.5$, the vertical symmetry plane of the punch (Figure 19d), $y = 1$, the vertical plane right beneath the punch (Figure 19e), $z = 0$, the bottom face of the box (Figure 19f), and the top face of the box (Figure 19g).

[104] We see that the pressure field shows a complicated three-dimensional spatial variation due to the hydrostatic pressure perturbed by the pressure imposed by the punch of roughly the same order of magnitude. This is clearly visible on the first cross section, where the left part of the image (away from the punch) shows a linear gradient while the

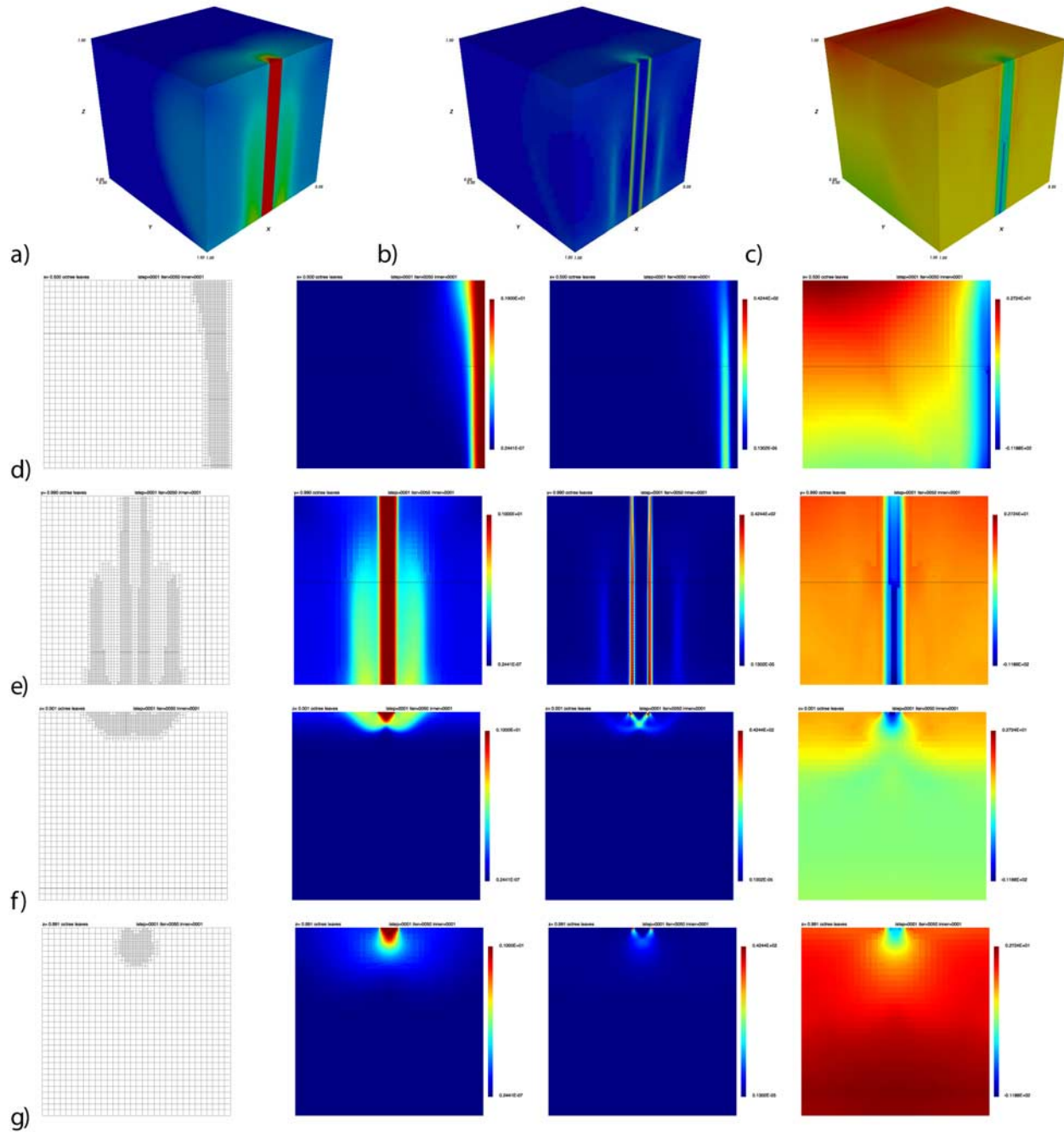


Figure 19. (a) Velocity norm field; (b) E_2' field; (c) pressure field; (d–g) cross sections of the grid, the velocity field, the E_2' field and the pressure field in planes $x = 0.5, y = 1, z = 0$, and $z = 1$.

right part beneath the punch shows a pressure field rather constant and close in magnitude to the one at the bottom.

[105] On the second cross section, the grid is refined in regions close to the punch area. It is highly irregular and we see that the capture of rigid blocks characterized by the two shear zones, one on each side of the punch, roughly takes place at half the height of the cube.

[106] At the bottom of the cube, the shear zones and velocity field look similar to the plane strain case, but due to the presence of the downward velocity field that also has to go around the punch area, the angle β is no more $\pi/4$ and the rotation regions no more quarter circles. The grid

reflects the geometry of the shear zones, and unrefined regions indicate the capture of rigid blocks.

[107] At the top of the cube, the pressure is null, which makes the Drucker-Prager criterion become equivalent to the von Mises, and yet we do not observe the typical shear zone pattern presented in this paper. This can be explained by the w component of the velocity field that increases with depth due to the gravity and that perturbs the system, preventing it from localizing properly the deformation. Accordingly, the grid is only refined close to the punch area but the refinement shows very little lateral extent as the deformation is diffuse. We also observe that the E_2' and $|v|$

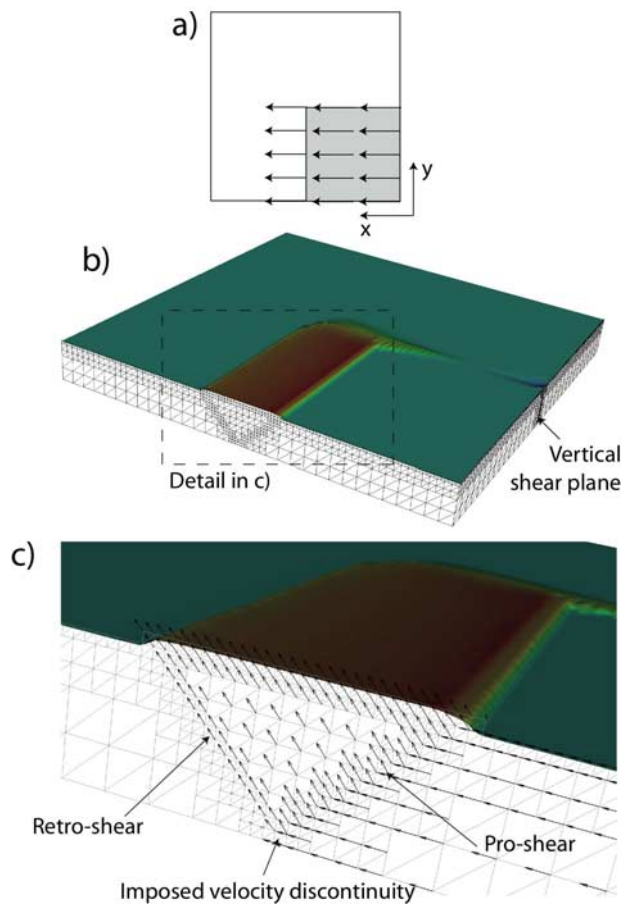


Figure 20. (a) Imposed velocity boundary conditions at the base of the unit cube; (b) octree and free surface after 30 timesteps; (c) closeup of the computed velocity field in the vicinity of the uplifting wedge bordered by the two shear bands.

fields show a vertical variation due to the yield criterion that depends on the pressure (and therefore on z).

5.5. Three-Dimensional Double-Vergent Critical Wedge

[108] Finally, in order to demonstrate the use and suitability of DOUAR to solve complex three-dimensional geodynamical problems, we have performed a numerical experiment at the scale of the Earth's crust, in which a basal velocity discontinuity drives shortening and thickening of the continental crust, assumed to behave plastically according to Mohr-Coulomb's failure criterion. This setting represents, to first order, the conditions experienced by the crust at the onset of continental collision driven by subduction of the underlying lithospheric mantle. This type of experiment has been performed in two dimensions (*Willett et al.* [1993] and *Beaumont et al.* [1994], among many others) and has led to the understanding of complex geodynamical situations [*Beaumont et al.*, 1996, 2000, 2001]. The predicted initial deformation pattern consists of two oppositely dipping shear bands that root in the imposed basal velocity discontinuity [*Willett et al.*, 1993]. Reverse movement on both structures leads to uplift of a nondeforming triangular wedge.

[109] In Figure 20, we present the results of a similar experiment performed with DOUAR. We have imposed a finite basal velocity field along one quarter of the unit cube (Figure 20a). In this way, the problem is three-dimensional and represents one of the ends of a finite-width collisional orogen. An interface representing the Earth's surface has been imbedded in the unit cube at a height of 0.1 from the base of the model. The parameters have been scaled to represent a crustal layer of 10 km thickness and 100×100 km lateral dimensions, characterized by a cohesion of 20 MPa, an angle of friction of 15° and a density of 2800 kg/m^3 . Strain softening leads to a progressive reduction of the angle of friction from 15 to 5° as deformation accumulates from 50 to 150%. The model was run for 30 time steps, leading to a total shortening of 1.5 km (15% of the crustal layer initial thickness).

[110] Using the progressive mesh refinement algorithm described in the previous sections, the geometry of the octree has evolved from a uniform discretization at level 5 to that shown in Figures 20b and 20c. Two refinement criteria have been used: one based on the intersection of the octree by the free surface, colored in Figure 20 as a function of elevation (or distance from its initial flat geometry), the other based on the computed velocity gradient. This has led to a refinement of the octree to the maximum allowed level (7) in the vicinity of the free surface and along the two shear planes that root into the velocity discontinuity. This refinement is well suited to track the geometry of the deforming free surface but, most importantly, to capture the large velocity gradient across both shear zones. Using the terminology introduced by *Willett et al.* [1993], we observe that the retroshear is characterized by a large variation in velocity amplitude (finite on one side, zero on the other), while the proshear is characterized by a strong variation in the direction of the velocity field. Note, however, that the triangular uplifting "plug" comprised between the two shear bands is characterized by a uniform velocity field; consequently it is not deforming and, thanks to the refinement algorithm, it is not refined beyond level 6. The imposed basal velocity also leads to a strong velocity gradient along a vertical plane aligned with the x direction at $y = 0.5$ which has led to a local refinement of the octree to level 7 (Figure 20b).

[111] Compared to a uniform refinement at level 7, this leads to a substantial reduction in the number of finite elements ($\sim 85,000$ of which $\sim 41,000$ are at level 7) and thus a nonnegligible economy in computation time, especially in this three-dimensional setup, without sacrificing the accuracy of the solution. During the first time step, the model converged after 15 nonlinear iterations; in subsequent time steps, the model converged after one iteration. In the final octree geometry, the solution of the finite element equations (factorization and back substitution) took approximately 2 s (wall time) on a 32 processor cluster.

[112] A complete description of the solution of this experiment is beyond the scope of this paper, as well as a more complete parameter sensitivity analysis, including the effect of increasing the basal temperature to trigger thermally activated creep near the base of the model, or the effect of eroding the free surface. This example clearly demonstrates, however, the capabilities of DOUAR in solving complex, three-dimensional geodynamical prob-

lems at a relatively low computational cost, thanks to the octree-based, grid refinement algorithm described in this manuscript.

Appendix A: Plane Strain Formulation

[113] Plane strain requires for instance $\dot{\epsilon}_{xx} = 0$ if we impose that flow of matter can only occur in the plane (yz). Equation (13) then implies $s_{xx} = 0$, or, recalling the definition of the deviatoric stress tensor:

$$\sigma_{xx} = \frac{1}{2}(\sigma_{yy} + \sigma_{zz}) \quad (\text{A1})$$

The flow rule then yields

$$\begin{aligned} \dot{\epsilon}_{yy} &= \lambda s_{yy} = \lambda \frac{1}{2}(\sigma_{yy} - \sigma_{zz}) \\ \dot{\epsilon}_{zz} &= \lambda s_{zz} = \lambda \frac{1}{2}(\sigma_{zz} - \sigma_{yy}) \\ \dot{\epsilon}_{yz} &= \lambda s_{yz} = \lambda \sigma_{yz} \end{aligned} \quad (\text{A2})$$

which, combined with equation (6) gives:

$$\frac{2\dot{\epsilon}_{yz}}{\dot{\epsilon}_{yy} - \dot{\epsilon}_{zz}} = \frac{\frac{\partial v}{\partial z} + \frac{\partial w}{\partial y}}{\frac{\partial v}{\partial y} - \frac{\partial w}{\partial z}} = \frac{2\sigma_{yz}}{\sigma_{yy} - \sigma_{zz}} \quad (\text{A3})$$

The von Mises yield criterion becomes

$$\frac{1}{4}(\sigma_{yy} - \sigma_{zz})^2 + \sigma_{yz}^2 - k^2 = 0 \quad (\text{A4})$$

and the mechanical equilibrium equation (10) transforms into

$$\frac{\partial \sigma_{yy}}{\partial y} + \frac{\partial \sigma_{yz}}{\partial z} = 0 \quad (\text{A5})$$

$$\frac{\partial \sigma_{yz}}{\partial y} + \frac{\partial \sigma_{zz}}{\partial z} = 0 \quad (\text{A6})$$

[114] Equations (A4), (A5), and (A6) form a system of three equations with three unknowns (σ_{yy} , σ_{zz} , σ_{yz}). If the boundary conditions are specified in terms of stresses, then such a problem is well posed, and the stress field can be statically determined. The velocity field can then be computed afterward with the remaining equations (8) and (A3).

Appendix B: Analytical Solution to the Two-Dimensional Punch

[115] There are many textbooks in which the derivation of the analytical solution to an half-infinite plastic medium indented by a flat die problem is carried out [Hill, 1950; Freundenthal and Geiringer, 1958; Kachanov, 2004], either through geometrical considerations and/or by means of the mathematical theory of hyperbolic equations and associated

characteristics. We shall hereafter present a brief rederivation of the solution.

[116] The indenter moves downward with a velocity w_p , and the deformations are assumed small so that changes in shape of the free surface can be ignored. There are no temperature changes nor body forces.

B1. Stress Field

[117] Let us call ψ the angle that an arbitrary direction \mathbf{m} makes with the positive y direction, and σ_m , τ_m the component of the stress tensor in the \mathbf{m} direction and normal to it, respectively. The counterclockwise rotation matrix \mathcal{R} of angle ψ is given by

$$\mathcal{R} = \begin{pmatrix} \cos \psi & -\sin \psi \\ \sin \psi & \cos \psi \end{pmatrix} \quad (\text{B1})$$

and the stress tensor in the rotated coordinate system is given by $\sigma' = \mathcal{R}\sigma\mathcal{R}^{-1}$, so that

$$\begin{aligned} \sigma_m &= \frac{\sigma_{yy} + \sigma_{zz}}{2} + \frac{\sigma_{yy} - \sigma_{zz}}{2} \cos 2\psi + \sigma_{yz} \sin 2\psi \\ \tau_m &= -\frac{\sigma_{yy} - \sigma_{zz}}{2} \sin 2\psi + \sigma_{yz} \cos 2\psi \end{aligned} \quad (\text{B2})$$

[118] The normal stress reaches its extremum values ($d\sigma/d\psi = 0$) for two values of ψ , $\psi' = \theta$ and $\psi'' = \theta + \pi/2$, where θ is defined by

$$\tan 2\theta = \frac{2\sigma_{yz}}{\sigma_{yy} - \sigma_{zz}} \quad (\text{B3})$$

[119] These are called principal directions, and along them the shear stress τ is null and the principal stresses are given by

$$\sigma_{1,2} = \frac{\sigma_{yy} + \sigma_{zz}}{2} \pm \sqrt{\left(\frac{\sigma_{yy} - \sigma_{zz}}{2}\right)^2 + \sigma_{yz}^2} \quad (\text{B4})$$

[120] On the other hand, the extrema $d\tau/d\psi$ of τ define two other directions $\psi^* = \phi$ and $\psi^{**} = \phi + \pi/2$ which are seen to bisect the angles of the principal directions, and are coined directions of maximum shear.

[121] Regarding the strain rate tensor, the directions of shear strain define the directions of the slip lines, and the corresponding normal strain rate vanishes in plane strain since $\dot{\epsilon} = (\dot{\epsilon}_{yy} + \dot{\epsilon}_{zz})/2 = 0$, from equation (8). These slip lines form two orthogonal families of curves shown as α and β lines.

[122] When $\psi = \theta$, then σ' is diagonal and the diagonal terms are σ_1 and σ_2 . Applying a rotation of angle $-\theta$ to σ' leads to the following well known formulae:

$$\begin{aligned} \sigma_{yy} &= \frac{\sigma_1 + \sigma_2}{2} + \frac{\sigma_1 - \sigma_2}{2} \cos 2\theta \\ \sigma_{zz} &= \frac{\sigma_1 + \sigma_2}{2} - \frac{\sigma_1 - \sigma_2}{2} \cos 2\theta \\ \sigma_{yz} &= \frac{\sigma_1 - \sigma_2}{2} \sin 2\theta \end{aligned} \quad (\text{B5})$$

[123] Also, recalling the definition of the pressure in equation (3), then $p = -(\sigma_1 + \sigma_2)$, and the yield criterion

then leads to $k^2 = (\sigma_1^2 - \sigma_2^2)/4$, or $k = (\sigma_1 - \sigma_2)/2$ since $\sigma_1 > \sigma_2$. Making a change of angle $2\varphi = 2\theta - \pi/2$, the equation (B5) then simply become

$$\sigma_{yy} = -p - k \sin 2\varphi \quad (\text{B6})$$

$$\sigma_{zz} = -p + k \sin 2\varphi \quad (\text{B7})$$

$$\sigma_{yz} = k \cos 2\varphi \quad (\text{B8})$$

[124] The three unknown stress components have been replaced by two unknown stress parameters p and φ . Substituting equations (B6), (B7), and (B8) into the mechanical equilibrium equations (A5) and (A6) gives

$$\begin{aligned} \frac{\partial p}{\partial x} + 2k \cos 2\varphi \frac{\partial \varphi}{\partial x} + 2k \sin 2\varphi \frac{\partial \varphi}{\partial y} &= 0 \\ \frac{\partial p}{\partial y} + 2k \sin 2\varphi \frac{\partial \varphi}{\partial x} - 2k \cos 2\varphi \frac{\partial \varphi}{\partial y} &= 0 \end{aligned} \quad (\text{B9})$$

[125] It can be shown that this system of equations in $p(x, y)$ and (x, y) is hyperbolic. In order to do so, we can show that there are two real families of characteristics whose property is to be that the first derivatives of p and φ may be discontinuous across them. One can express the differentials dp and d as follows:

$$\begin{aligned} dp &= \frac{\partial p}{\partial x} dx + \frac{\partial p}{\partial y} dy \\ d\varphi &= \frac{\partial \varphi}{\partial x} dx + \frac{\partial \varphi}{\partial y} dy \end{aligned} \quad (\text{B10})$$

and by treating them as a set of linear algebraic equations, equations (B9) and (B10) form a system of four equations with four unknowns

$$\begin{pmatrix} dx & dy & 0 & 0 \\ 0 & 0 & dx & dy \\ 1 & 0 & 2k \cos 2\varphi & 2k \sin 2\varphi \\ 0 & 1 & 2k \sin 2\varphi & -2k \cos 2\varphi \end{pmatrix} \begin{pmatrix} \frac{\partial p}{\partial x} \\ \frac{\partial p}{\partial y} \\ \frac{\partial \varphi}{\partial x} \\ \frac{\partial \varphi}{\partial y} \end{pmatrix} = \begin{pmatrix} dp \\ d\varphi \\ 0 \\ 0 \end{pmatrix} \quad (\text{B11})$$

[126] The derivatives will be uniquely specified unless the determinant Δ of the coefficient matrix is null. When solving for $\Delta = 0$, one obtains a quadratic equation in dy/dx that has two roots:

$$\left. \frac{dy}{dx} \right|_1 = \tan \varphi \quad \text{and} \quad \left. \frac{dy}{dx} \right|_2 = \tan(\varphi + \pi/2) \quad (\text{B12})$$

[127] These last relations define two orthogonal lines, or characteristics passing through each point, which coincide with the slip lines.

[128] When the x and y axes are tangential to the α and β slip lines, then $\varphi = 0$ and equation (B9) become:

$$\begin{aligned} \frac{\partial p}{\partial x} + 2k \frac{\partial \varphi}{\partial x} &= 0 \\ \frac{\partial p}{\partial y} - 2k \frac{\partial \varphi}{\partial y} &= 0 \end{aligned} \quad (\text{B13})$$

or,

[129] $p + 2k\varphi$ is constant along an α line

[130] $p - 2k\varphi$ is constant along a β line

[131] These relations are the Hencky equations.

B2. Velocity Field

[132] Having solved the equations for the stresses, one can now solve for the velocity field. The coaxiality condition (A3) combined with equation (B3) yields

$$\frac{\partial v}{\partial y} \cos 2\varphi + \frac{\partial v}{\partial z} \sin 2\varphi + \frac{\partial w}{\partial y} \sin 2\varphi - \frac{\partial w}{\partial z} \cos 2\varphi = 0 \quad (\text{B14})$$

[133] Similarly to the previous part, one can take the differentials dv and dw and coupling these with equations (8) and (B14), a system of four equations with four unknowns ($\partial_y v$, $\partial_z v$, $\partial_y w$, $\partial_z w$) is obtained. Again the first derivatives may be discontinuous across the curves defined by equation (B12) and therefore the velocity characteristics coincide with the previously calculated slip lines. Taking $\varphi = 0$ in equation (B14) and considering the incompressibility condition leads to

$$\partial_y v|_{\varphi=0} = \partial_z w|_{\varphi=0} = 0, \quad (\text{B15})$$

i.e., the rate of extension along a slip line is zero.

[134] Finally, let (v_α, v_β) be the velocity components in the slip line coordinate system. One can write

$$\begin{aligned} v &= v_\alpha \cos \varphi - v_\beta \sin \varphi \\ w &= v_\alpha \sin \varphi + v_\beta \cos \varphi \end{aligned} \quad (\text{B16})$$

and substituting these in equation (B15) with $\varphi = 0$ leads to

$$\begin{aligned} \frac{\partial v_\alpha}{\partial y} - v_\alpha \frac{\partial \varphi}{\partial y} &= 0 \\ \frac{\partial v_\beta}{\partial y} - v_\alpha \frac{\partial \varphi}{\partial y} &= 0 \end{aligned} \quad (\text{B17})$$

or,

[135] $dv_\alpha - v_\beta d\varphi = 0$ along an α line

[136] $dv_\beta + v_\alpha d\varphi = 0$ along a β line

[137] These are the Geiringer equations.

B3. Nonuniqueness of the Solution

[138] On Figure 1a is shown Prandtl's solution of slip lines. Suppose that the distribution of stresses is uniform under the indenter. As the surfaces of the indenter and the plastic medium are flat, the shear stress is null. The slip lines then make an angle $\pi/4$ to the surface and delimit three triangles Δ_{ACB} , Δ_{AFG} and Δ_{BDE} . Two curved domains

Υ_{AFC} and Υ_{BCD} connect these triangles. The velocity of the rigid wedge Δ_{ACB} is uniform and equal to w_p , while in all other domains the velocity modulus is $w_p/\sqrt{2}$, leading to a velocity discontinuity along AC and CB .

[139] On Figure 1b is shown Hill's solution to a rigid frictionless flat die indenting a rigid plastic half space. In this case no rigid wedge is present under the indenter: Δ_{OCB} and Δ_{AFO} are two smaller rigid wedges with velocity $w_p/\sqrt{2}$. In contrast with Prandtl's solution, the velocity field is then continuous in the plastic regions. It was later shown by Prager that it is possible to construct acceptable solutions to this problem as a combination of Prandtl and Hill mechanisms.

B4. Pressure Under the Indenter

[140] Since the slip lines in Δ_{ACB} are straight, then the stress is constant in this region. Let us consider the slip line passing through points M and N. At point N, $\varphi_N = \pi/4$, so that equation (B8) is automatically verified: $\sigma_{yz}|_N = 0$. Then, since no body force is applied, $\sigma_{zz}|_N = 0$ and one way to satisfy equation (B7) at point N is to set $p = k$. Finally equation (B6) yields $\sigma_{yy}|_N = -2k$.

[141] Along this α slip line, the Hencky equation holds so that

$$p_M + 2k\varphi_M = p_N + 2k\varphi_N \quad (\text{B18})$$

At point M, $\varphi|_M = -\pi/4$, leading to $p_M = k(1 + \pi)$. Using the equations (B6), (B7), and (B8) leads to

$$\begin{aligned} \sigma_{yy}|_M &= -k\pi \\ \sigma_{zz}|_M &= -k(2 + \pi) \\ \sigma_{yz}|_M &= 0 \end{aligned} \quad (\text{B19})$$

[142] **Acknowledgments.** The work described in this paper has been supported by an ARC (Australian Research Council) Discovery grant. C. Thieulot was supported by a postdoctoral fellowship from the Canadian Institute for Advanced Research. Computations were performed on a cluster cofinanced by Rennes-Metropole, the Centre National de la Recherche Scientifique (CNRS), the Agence Nationale de la Recherche (ANR), and a Marie Curie International Reintegration Grant of the European Union.

References

Amestoy, P., I. Duff, and J.-Y. L'Excellent (2000), Multifrontal parallel distributed symmetric and unsymmetric solvers, *Comput. Methods Appl. Mech. Eng.*, *184*, 501–520.

Arrow, K., L. Hurwicz, and H. Uzawa (1968), *Studies in Nonlinear Programming*, Stanford Univ. Press, Stanford, Calif.

Bathe, K.-J. (1982), *Finite Element Procedures in Engineering Analysis*, Prentice-Hall, Upper Saddle River, N. J.

Beaumont, C., P. Fullsack, and J. Hamilton (1994), Styles of crustal deformation in compressional orogens caused by subduction of the underlying lithosphere, *Tectonophysics*, *232*, 119–132.

Beaumont, C., P. Kamp, J. Hamilton, and P. Fullsack (1996), The continental collision zone, South Island, New Zealand: Comparison of geodynamical models and observations, *J. Geophys. Res.*, *101*, 3333–3359.

Beaumont, C., J. Munoz, J. Hamilton, and P. Fullsack (2000), Factors controlling the alpine evolution of the central pyrenees inferred from a comparison of observations and geodynamical models, *J. Geophys. Res.*, *105*, 8121–8145.

Beaumont, C., R. Jamieson, M. Nguyen, and B. Lee (2001), Himalayan tectonics explained by extrusion of a low-viscosity crustal channel coupled to focused surface denudation, *Nature*, *414*, 738–742.

Belytschko, T., Y. Lu, and L. Gu (1994), Element-free galerkin methods, *Int. J. Numer. Methods Eng.*, *37*, 229–256.

Benzi, M., G. H. Golub, and J. Liesen (2005), Numerical solution of saddle point problems, *Acta Numer.*, *14*, 1–137.

Bochev, P. B., C. R. Dohrmann, and M. D. Gunzburger (2006), Stabilization of low-order mixed finite elements for the Stokes equations, *SIAM J. Numer. Anal.*, *44*(1), 82–101.

Bolton, M., and C. Lau (1993), Vertical bearing capacity factors for circular and strip footings on Mohr-Coulomb soil, *Can. Geotech. J.*, *30*, 1024–1033.

Brace, W., and D. Kohlstedt (1980), Limits on lithospheric stress imposed by laboratory experiments, *J. Geophys. Res.*, *85*, 6248–6252.

Braun, J. (1993), Three-dimensional numerical modelling of compressional orogens: Thrust geometry and oblique convergence, *Geology*, *21*, 153–156.

Braun, J., and M. Sambridge (2002), A numerical method for solving partial differential equations on highly irregular evolving grids, *Nature*, *376*, 655–660.

Braun, J., J. Chéry, A. Poliakov, D. Mainprice, A. Vauchez, A. Tomassi, and M. Daignières (1999), A simple parameterization of strain localization in the ductile regime due to grain-size reduction: A case study for olivine, *J. Geophys. Res.*, *104*, 25,167–25,181.

Braun, J., C. Thieulot, P. Fullsack, M. DeKool, and R. Huisman (2008), Douar: a new three-dimensional creeping flow model for the solution of geological problems, *Phys. Earth Planet. Inter.*, *171*, 76–91, doi:10.1016/j.pepi.2008.05.003.

Carter, N. (1975), High temperature flow of rocks, *Rev. Geol. Geophys.*, *13*, 344–349.

Chen, S., Y. Liu, and Z. Cen (2008), Lower bound shakedown analysis by using the element free galerkin method and non-linear programming, *Comput. Methods Appl. Mech. Eng.*, *197*, 3911–3921, doi:10.1016/j.cma.2008.03.009.

Christiansen, E., and K. D. Andersen (1999), Computation of collapse states with von mises type yield condition, *Int. J. Numer. Methods Eng.*, *46*, 1185–1202.

Christiansen, E., and O. S. Pedersen (2001), Automatic mesh refinement in limit analysis, *Int. J. Numer. Methods Eng.*, *50*, 1331–1346.

Coulomb, C. A. (1773), Essai sur une application des règles de maximis et minimis à quelques problèmes de statique relatifs à l'architecture, *Mem. Acad. R. Pres. Divers Savants*, *7*, 343–382.

Drucker, D., and W. Prager (1952), Soil mechanics and plastic analysis or limit design, *Q. Appl. Math.*, *10*(2), 157–165.

Erickson, H., and A. Drescher (2002), Bearing capacity of circular footings, *J. Geotech. Geoenviron. Eng.*, *128*, 38–43.

Freudenthal, A. M., and H. Geiringer (1958), The mathematical theory of the inelastic continuum, in *Encyclopedia of Physics*, vol. VI, edited by S. Flügge, pp. 229–433, Springer, New York.

Frydman, S., and H. J. Burd (1997), Numerical studies of bearing capacity factor n_v , *J. Geotech. Geoenviron. Eng.*, *123*(1).

Fullsack, P. (1995), An arbitrary lagrangian-eulerian formulation for creeping flows and its application in tectonic models, *Geophys. J. Int.*, *120*, 1–23.

Gourvenec, S., M. Randolph, and O. Kingsnorth (2006), Undrained bearing capacity of square and rectangular footings, *Int. J. Geomech.*, *6*, 147–157.

Govers, R., and M. Wortel (2005), Lithosphere tearing at step faults: response to edges of subduction zones, *Earth Planet. Sci. Lett.*, *236*(1–2), 505–523.

Gupta, A. (2000), Wsmv: Watson sparse matrix package (part-ii: direct solution of general sparse systems), *Tech. Rep. RC 21888 (98472)*, IBM T.J. Watson Res. Cent.

Hill, R. (1950), *The Mathematical Theory of Plasticity*, Oxford Univ. Press, New York.

Houseman, G., and P. England (1993), Crustal thickening versus lateral expulsion in the Indian-Asian continental collision, *J. Geophys. Res.*, *98*, 12,333–12,249.

Hughes, T. J. (2000), *The Finite Element Method. Linear Static and Dynamic Finite Element Analysis*, Dover, Mineola, N. Y.

Huh, H., C. H. Lee, and W. H. Yang (1999), A general algorithm for plastic flow simulation by finite element limit analysis, *Int. J. Solids Struct.*, *36*, 1193–1207.

Kachanov, L. (2004), *Fundamentals of the Theory of Plasticity*, Dover, Mineola, N. Y.

Lee, J., R. Salgado, and S. Kim (2005), Bearing capacity of circular footings under surcharge using state-dependent finite element analysis, *Comput. Geotech.*, *32*, 445–457.

Lyamin, A. V., and S. W. Sloan (2002), Upper bound limit analysis using finite elements and non-linear programming, *Int. J. Numer. Anal. Methods Geomech.*, *26*, 181–216.

Moresi, L., and V. Solomatov (1998), Mantle convection with a brittle lithosphere: Thoughts on the global tectonics styles of the earth and venus, *Geophys. J. Int.*, *133*, 669–682.

Ngo, N., and F. Tin-Loi (2007), Shakedown analysis using the p-adaptive finite element method and linear programming, *Eng. Struct.*, *29*, 46–56.

- Owen, D., and E. Hinton (1980), *Finite Elements in Plasticity*, Pineridge, Swansea, U. K.
- Paterson, M. (1978), *Experimental Rock Deformation: The Brittle Field*, Springer, New York.
- Poirier, J.-P. (1980), Shear localization and shear instability in materials in the ductile field, *J. Struct. Geol.*, 2, 135–142.
- Regenauer-Lieb, K., R. Weinberg, and G. Rosenbaum (2006), The effect of energy feedbacks on continental strength, *Nature*, 442, 67–70.
- Taiebat, H., and J. Carter (2002), Bearing capacity of strip and circular foundations on undrained clay subjected to eccentric loads, *Geotechnique*, 52, 61–64.
- Tanner, R., and E. Tanner (2003), Heinrich hencky: a rheological pioneer, *Rheol. Acta*, 42, 93–101.
- Terzaghi, K. (1943), *Theoretical Soil Mechanics*, John Wiley, New York.
- Tin-Loi, F., and N. Ngo (2003), Performance of the p-version finite element method for limit analysis, *Int. J. Mech. Sci.*, 45, 1149–1166.
- Tresca, H. (1864), Sur l'écoulement des corps solides soumis à de fortes pressions, *C. R. Acad. Sci.*, 59, 754.
- von Mises, R. (1913), Mechanik der festen korper im plastisch deformablen zustand, *Nachr. K. Ges. Wiss.*, 1, 582–592.
- Willett, S. (1992), Dynamic and kinematic growth and change of a coulomb wedge, in *Thrust Tectonics*, edited by K. McClay, pp. 19–31, Chapman and Hall, London.
- Willett, S., C. Beaumont, and P. Fullsack (1993), Mechanical model for the tectonics of doubly vergent compressional orogens, *Geology*, 21, 371–374.
- Yu, X., and F. Tin-Loi (2006), A simple mixed finite element for static limit analysis, *Comput. Struct.*, 84, 1906–1917.
- Zienkiewicz, O., and R. Taylor (2002), *The Finite Element Method*, vol. 2, *Solid Mechanics*, 5th ed., Butterworth-Heinemann, New York.
- Zienkiewicz, O., M. Pastor, and M. Huang (1995), Softening, localisation and adaptive remeshing. Capture of discontinuous solutions, *Comput. Mech.*, 17, 98–106.

J. Braun and C. Thieulot, Géosciences Rennes, Université de Rennes 1, Rennes CEDEX F-CS35042, France. (jean.braun@univ-rennes1.fr)

P. Fullsack, Oceanography Department, Dalhousie University, Halifax, NS B3H 4J1, Canada. (philippe.fullsack@dal.ca)